

Seismic structure of the St. Paul Fracture Zone and Late Cretaceous to Mid Eocene oceanic crust in the equatorial Atlantic Ocean near 18°W

Kevin Growe^{1,2}, Ingo Grevemeyer¹, Satish C. Singh², Milena Marjanović², Emma P. M. Gregory², Cord Papenberg¹, Venkata Vaddineni², Laura Gómez de la Peña¹, and Zhikai Wang²

¹GEOMAR Helmholtz Centre for Ocean Research Kiel

²Université de Paris, Institut de Physique du Globe de Paris; CNRS, Paris, France

Corresponding author: Kevin Growe (kevin.growe93@web.de)

Key Points:

- Seismic structure along the St. Paul fracture zone reflects magmatically accreted oceanic crust
- Oceanic crust across St. Paul shows only small thickness variations, lacking evidence for regional crustal thinning near fracture zones
- Magmatic nature of crust supports a mechanism where transform crust is augmented before being turned into a fracture zone

Abstract

Plate tectonics characterize transform faults as conservative plate boundaries where the lithosphere is neither created nor destroyed. In the Atlantic, both transform faults and their inactive traces, fracture zones, are interpreted to be structurally heterogeneous, representing thin, intensely fractured, and hydrothermally altered basaltic crust overlying serpentinized mantle. This view, however, has recently been challenged. Instead, transform zone crust might be magmatically augmented at ridge-transform intersections before becoming a fracture zone. Here, we present constraints on the structure of oceanic crust from seismic refraction and wide-angle data obtained along and across the St. Paul fracture zone near 18°W in the equatorial Atlantic Ocean. Most notably, both crust along the fracture zone and away from it shows an almost uniform thickness of 5-6 km, closely resembling normal oceanic crust. Further, a well-defined upper mantle refraction branch supports a normal mantle velocity of 8 km/s along the fracture zone valley. Therefore, the St. Paul fracture zone reflects magmatically accreted crust instead of the anomalous hydrated lithosphere. Little variation in crustal thickness and velocity structure along a 200 km long section across the fracture zone suggests that distance to a transform fault had negligible impact on crustal accretion. Alternatively, it could also indicate that a second phase of magmatic accretion at the proximal ridge-transform intersection overprinted features of starved magma supply occurring along transform faults.

Plain Language Summary

Transform faults are tectonic plate boundaries where the lithosphere is neither created nor destroyed. Previous studies have revealed that many Atlantic transform faults and their inactive traces, fracture zones, are characterized by a strongly altered and fractured crust that is reduced in thickness and is overlying altered mantle rocks. Conversely, recent results propose a mechanism of secondary magma supply at the ridge-transform intersections, that enhances the crust while being transferred from the transform fault to the fracture zone domain. Here, we present results from seismic experiments along and across the St. Paul fracture zone near 18°W in the equatorial Atlantic Ocean. We observe a nearly uniform crustal thickness of 5-6 km and waves traveling through the upper mantle with a velocity of 8 km/s. Both observations indicate a magmatic formation of the crust and the absence of strong alteration of the upper mantle. The relatively constant crustal thickness and little variation in seismic velocities along the 200 km long profile across the fracture zone suggests that the distance to the transform fault had no significant impact on the crustal formation process. Alternatively, secondary magma supply at the ridge-transform intersection enhancing the crust could overprint effects from any anomalous formation conditions.

1 Introduction

Plate tectonics separates Earth's surface into rigid plates (McKenzie, 1967; Morgan, 1968), and deformation or relative motion between plates reveals three different types of oceanic plate boundaries: (i) constructive plate boundaries at mid-ocean ridges (MOR) where new seafloor is created, (ii) destructive plate boundaries at subduction zones where the oceanic lithosphere is transferred into the mantle and recycled, and (iii) conservative plate boundaries

and hence transform faults (TF) where the lithosphere is neither created nor destroyed as plates move past each other (Morgan, 1968). In ocean basins, transform faults offset MOR by tens to several hundreds of kilometers (Searle et al., 1994), splitting them into first-order spreading segments (Macdonald et al., 1988). They are long-lived features, and in the equatorial Atlantic, the largest transform faults, namely Chain, Romanche, and St. Paul, can be followed along their inactive traces, called fracture zones (FZ), towards the margins of the Atlantic Ocean (Wilson, 1965). Fracture zones are prominent linear features on the ocean floor that were identified and named before plate tectonics linked them to seafloor spreading (Menard, 1955; 1967).

Oceanic crust formed along a spreading ridge is generally believed to remain largely unchanged as it is moved by plate motion away from the active plate boundary. Its structure can be best described with respect to a layered structure, where the crust is divided into two main distinct lithologic layers exhibiting different seismic properties (e.g., Raitt, 1963). The upper crust (layer 2) consists of pillow basalts overlaying a basaltic sheeted dike complex (e.g., Vine & Moores, 1972) and reveals high velocity gradients of 1-2 s⁻¹ and velocities from 3-5 km/s just below the basement to 6.3-6.8 km/s at a depth of 1-2 km below the basement (e.g., Grevemeyer et al., 2018; White et al. 1992; Whitmarsh, 1978). The mid- and lower crust (layer 3) instead consist of plutonic, mostly gabbroic, rocks and has low velocity gradients of 0.1-0.2 s⁻¹ and velocities from ~6.6 km/s at the top of the layer to 7.2 km/s at its base (e.g., Carlson & Miller, 2004; Vine & Moores, 1972). The thickness of layer 3 is much more variable than the thickness of layer 2 such that variations in crustal thickness in several studies are related to thickness variations of layer 3 (e.g., Mutter & Mutter, 1993).

It has long been recognized that oceanic crust varies along spreading segments, with the thickest crust formed at a segment center away from major ridge crest discontinuities and the thinnest crust at segment ends or transform faults (e.g., Macdonald et al., 1988; Tolstoy et al., 1993). Along fast-spreading ridges, thickness variations are reasonably small, within some hundreds of meters to less than a kilometer (e.g., Canales et al., 2003). At slow- and ultraslow-spreading ridges, crust of ~7-9 km thickness may occur at segment centers and decrease to only 4-6 km at segment ends (e.g., Canales et al., 2000; Dannowski et al., 2011; Grevemeyer et al., 2018; Niu et al., 2015). These along-axis thickness variations can be best explained by focused mantle upwelling at segment centers and lateral melt transport, suggesting that mantle upwelling is intrinsically plume-like (3-D) beneath a slow-spreading ridge but more sheet-like (2-D) beneath a fast-spreading ridge (Bell & Buck, 1992; Lin & Morgan, 1992).

Along-axis changes in oceanic crustal architecture suggest that the end of spreading segments and hence transform faults represent the magmatically starved end-member of the oceanic crust (e.g., Detrick et al., 1993; White et al., 1984) where tectonic stresses rotate by tens of degrees over a very short distance (Morgan & Parmentier, 1984), changing from normal faulting at the spreading axis to strike-slip along the transform (e.g., Sykes, 1967). In the Pacific, the crustal structure at transform faults reveals a drop of seismic P-wave velocity in the active strike-slip fault, indicating the presence of high porosities along the tectonically active fault trace (Roland et al., 2012). However, it shows little evidence for reduced melt supply as crustal thickness across the fast-slipping transforms indicates only a small reduction, which is in the order of some hundreds of meters (Roland et al., 2012). In contrast, some transform faults in the Atlantic exhibit thin crust ~4-5 km thick (e.g., Ambos & Hussong, 1986; Detrick et al., 1982; Whitmarsh & Calvert, 1986) along transform valleys which is 1-2 km thinner when compared to the neighboring normal oceanic crust (e.g., Grevemeyer et al., 2018; van Avendonk et al., 2017;

White et al., 1992). The above observations led to the conclusion that lithosphere along transform faults and fracture zones might be intensely fractured, faulted, and composed of hydrothermally altered basaltic and gabbroic rocks overlying ultramafics that might be extensively serpentinized (Detrick et al., 1993; White et al., 1984).

A recent study suggests that the crust beneath the Chain fracture zone in the equatorial Atlantic region has a nearly normal crustal thickness (Marjanović et al., 2020). This observation has been independently supported using global bathymetric observations and numerical simulation on transform fault tectonics (Grevemeyer et al., 2021) suggesting that crust is (i) initially magmatically emplaced near a ridge-transform intersection (RTI), (ii) experiences tectonic deformation, and extension while being moved along the transform fault and (iii) finally it is augmented by the second stage of magmatism as it passes the opposing RTI. If correct, the formation of crust at transform faults should occur in three distinctive phases, suggesting that the structure of crust present below the valley of an active transform fault should differ profoundly from crust found along its fracture zones.

Here, we use two state-of-the-art seismic profiles shot in 2017 and 2018 with modern seismic refraction and wide-angle equipment surveying the St. Paul fracture zone near 18°W in the equatorial Atlantic region (Fig. 1). The seismic data are well-suited for seismic tomography in order to study the structure along a 140 km-long roughly west-east running profile in the valley of the St. Paul fracture zone and along a 300 km-long north-south trending profile crossing the fracture zone and sampling the adjacent mature oceanic crust. The north-south striking profile runs parallel to the trend of the Mid-Atlantic Ridge (MAR) and hence should reveal features governed by changes in melt supply towards a transform fault and lateral melt transport, which is expected to diminish when approaching transform faults (e.g., Lin et al., 1990; Macdonald et al., 1988; White et al., 1984). The crustal and upper mantle velocity structures are derived from a joint tomographic inversion of first arrival travel times and wide-angle reflections from the crust-mantle boundary, providing high-resolution constraints on the seismic velocity structure and crustal thickness along the fracture zone and the dependence of crustal accretion as a function of distance to a fracture zone.

2 Regional Setting of the St. Paul Fracture Zone and Study Area

2.1 Regional Setting of the St. Paul Fracture Zone

The St. Paul fracture zone (SPFZ) is one of the major east-west striking equatorial fracture zones of the Atlantic Ocean. At the active MAR, the St. Paul, Romanche and Chain transform faults offset the ridge crest by ~1800 km, causing an age variation of 90 Myr over 400 km north-south distance (Müller et al., 2008). The active domain of the St. Paul transform fault system offsets the MAR by ~600 km and can be subdivided into four strike-slip faults; sandwiched in between are three short intra-transform spreading segments (Fig. 1a). Maia et al. (2016) studied the northern TF segment and found a complex tectonic regime revealing a transpressional zone exhuming deformed and serpentinized mantle rocks, triggered as a response to a change of relative plate motion ~11 Myr ago. The fossil trace of the transform fault, the fracture zone can be followed using the vertical gravity gradient (Sandwell et al., 2014) across the entire Atlantic Ocean, from the continental shore of Liberia in the east to the Amazonas Basin in the west, resulting in a total length of ~3000 km. For ages greater than 20 Myr (Mueller et al., 2008) away from both RTI, the bathymetry data indicate the presence of only two fracture zone valleys, suggesting that today's complex transform-fault-system developed roughly 20 Myr ago.

Using 2-D ultra-deep multichannel seismic reflection data, Mehouchi and Singh (2018) imaged the lithosphere-asthenosphere boundary along a north-south striking line and revealed a southward thinning of the lithosphere, mimicking the age contrast across the system of fracture zones at ~18°W.

2.2 Study Area

Within our study area, ~680 km east from the active St. Paul transform fault system (Fig. 1a), the ~10 km wide northernmost St. Paul fracture zone valley (SPFZ-1) separates ~70 Ma oceanic lithosphere in the north from 40-50 Ma lithosphere in the south (Müller et al., 2008). Here, the valley is covered by sediments up to a kilometer thick, creating a smooth surface but still forming a 200-300 m deep valley with respect to the surrounding ocean floor (Fig. 1c). Its younger southern edge is flanked by significantly rougher bathymetry, revealing ridge-like features aligned mostly perpendicular to the FZ that we interpret as overshooting ridges, as observed near RTIs globally (e.g., Grevemeyer et al., 2021; Lonsdale, 1986; Marjanović et al., 2020). The older northern flank of the FZ can be subdivided into two distinct domains (Fig 1c). The north-western area to the west of the intersection of seismic profiles shows ridge- and dome-like features mostly parallel to the fracture zone. In contrast, the north-eastern domain reveals a rather smooth seafloor, except for a seamount-like structure located at the eastern limit of the west-east striking seismic line LI-02.

The north-south striking seismic line IS-01 ran over a smooth seafloor of an almost constant depth to the north of St. Paul, except for two ridge-like features near OBS 1 and OBS 5 (Fig 1b). The bathymetry to the south of SPFZ-1 is significantly rougher, showing east-west trending ridge-like features separating SPFZ-1 from a second, parallel fracture zone valley in the south (SPFZ-2) near OBS13. SPFZ-2 is related to the southernmost TF segment of the modern active TF system of St. Paul (Fig. 1a). The seismic line is limited in the south by another FZ parallel ridge south of SPFZ-2 and a deep basin just north of the Romanche TF (Fig. 1a, b).

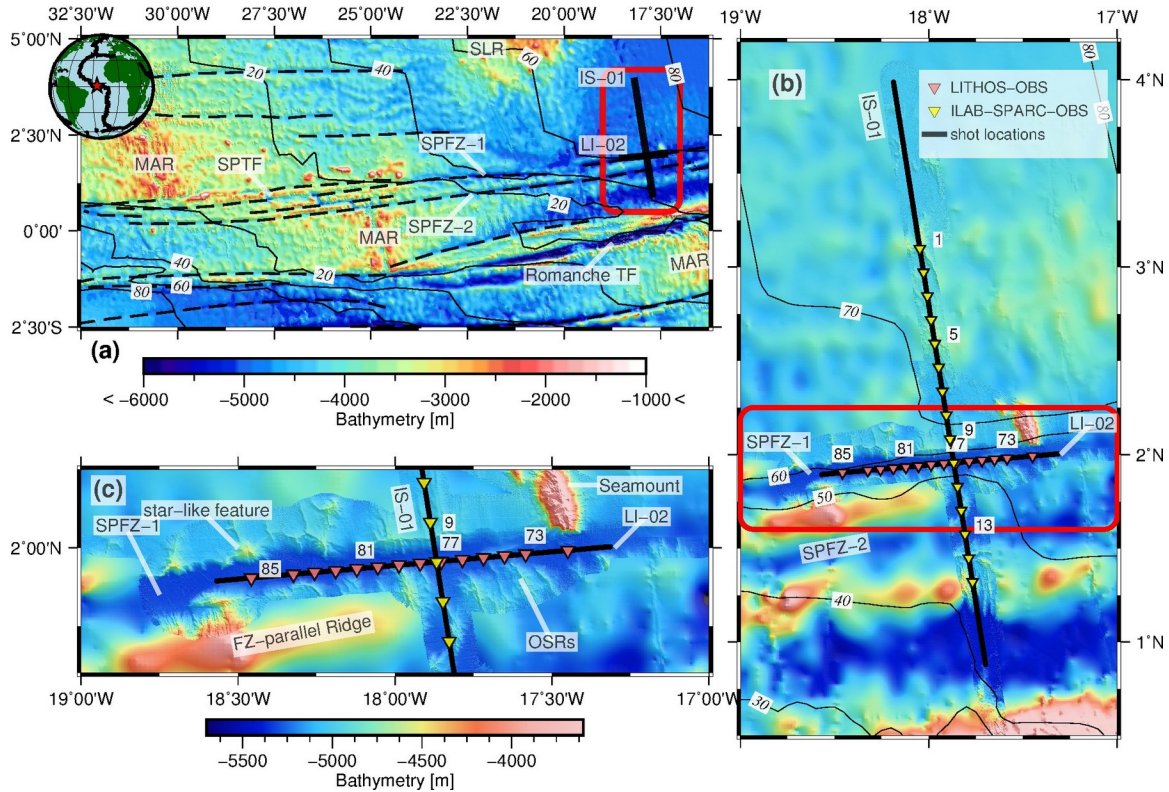


Figure 1: Regional and survey map in the equatorial Atlantic Ocean. **(a)** Bathymetric map showing survey location and tectonic setting around the SPFZ. The bathymetry is from TOPEX satellite gravity data (Sandwell et al., 2014). Thin labelled black lines denote crustal age after Müller et al. (2008) with an interval of 20 Myrs. Dashed lines denote fracture zones mapped by Matthews et al. (2011). Plate boundaries on inset globe are from Bird (2003) and red star indicates the survey location. The thick black lines represent the two survey lines (LI-02 and IS-01). Red box marks the survey area shown in (b). The main regional tectonic features are labeled (see definition of acronyms at the end of the caption). **(b)** Survey area showing shot and OBS locations for both seismic lines (note legend). Every fourth OBS is labeled. The bathymetry is combined by TOPEX data and acquired shipboard high resolution multibeam echo-sounder data (LITHOS: 100x100 m; ILAB-SPARC: 50x50 m). The crustal ages are indicated by thin black contours and labelled with an interval of 10 Myrs. The red box depicts the closeup map shown in (c). **(c)** Closeup of bathymetric map of the surveyed transect of the SPFZ-1 using the same color scale as in (b). Prominent bathymetric features are labeled. Remaining features are displayed as in (b). Acronyms: MAR - Mid-Atlantic Ridge, TF - Transform Fault, SPTF - St. Paul Transform Fault, SPFZ - St. Paul Fracture Zone, SLR - Sierra Leone Rise, OSRs - Overshooting Ridges.

3 Data Acquisition and Processing

In the framework of the Trans-Atlantic-iLAB and LITHOS projects, several OBS based seismic refraction lines, as well as multichannel seismic reflection lines, were acquired during three cruises in the central equatorial Atlantic Ocean from 2015-2018. In this study, we present the results from the two seismic refraction and wide-angle profiles along and across the St. Paul fracture zone, at 2°N/18° W, hereafter named as profiles LI-02 and IS-01 (see Supplementary Figs S1 and S2). Profile IS-01 is coincident with the seismic reflection profile of Mehouchi and Singh (2018).

3.1 Acquisition LI-02

Profile LI-02 was acquired during the LITHOS cruise onboard the German R/V Maria S. Merian in December 2017, where 12 four-component ocean bottom seismometers (OBS) and two one-component ocean bottom hydrophones (OBH) with a spacing of 7.5 - 15 km were deployed within the fracture zone valley (Fig. 1c). For simplicity, we will refer to all receiver types as OBS. A total of 875 shots were fired at 210 bars on a 142 km long east-west orientated transect. A shot time interval of 90 s with a vessel speed of ~3.5 knots led to an average spatial shot interval of ~160 m. The two airgun sub-arrays each consisted of six G-guns, provided a total volume of 86 l, and were towed at a depth of 7.5 m. The OBS data were sampled at 250 Hz. All instruments recorded good quality data containing crustal (Pg) and mantle (Pn) refraction arrivals up to offsets of 90 km, and all but two OBS, OBS 82 and 85, also recorded wide-angle reflections from the Moho (PmP) (Fig. 2). Pg and PmP arrivals could be picked mostly between 5-25 and 15-30 km offsets, respectively. Pn arrivals could be picked mostly up to 60 km offset and even up to 80-90 km for some record sections (see all record sections in Figures S1a-n in the supplementary material). Since no streamer data were acquired along the profile, the basement depth and the sediment structures were obtained by mirror imaging (Supplementary material Fig. S3) of the hydrophone component of OBS receiver gathers (e.g., Grion et al., 2007).

219 3.2 Acquisition IS-01

220 Line IS-01 is the northernmost part of the north-south profile acquired during the ILAB-SPARC
221 cruise aboard the French R/V Pourquoi Pas? in 2018. The profile is in total 850 km-long,
222 crossing farther south the Romanche transform fault ($\sim 0^\circ\text{N}$) (Gregory et al., 2021) and the Chain
223 fracture zone ($\sim 2^\circ\text{S}$) (Marjanović et al., 2020). Here, we use the data from the northernmost 350
224 km of the line containing 15 four-component OBS with an average instrument spacing of 14.2
225 km. The OBS data were sampled at 250 Hz. Most OBS receiver gathers provide good quality
226 data where both refraction and wide-angle reflection arrivals can be identified with confidence
227 (Fig. 2). Pg and PmP arrivals were picked mostly between 5-25 and 15-35 km offset,
228 respectively. Pn arrivals could be picked mostly up to 50 km offset (Fig. S2). A summary of the
229 acquisition parameters for the two refraction profiles is provided in Table S1.

230 A total of 1168 shots were fired at a pressure of 140 bars and at a source interval of 300 m. The
231 larger shot interval was chosen to minimize the noise level in the water column for later arrivals.
232 Two sub-arrays containing eight G-guns each provided a total volume of 82 liters and were
233 towed at a depth of 10 m. Real-time source monitoring provided excellent conditions for a well-
234 tuned signal which is critical for such an experiment.

235 Simultaneously, a 6 km-long streamer containing 960 hydrophones, grouped with a spacing of
236 6.25 m, was towed at a depth of 12 m to acquire multi-channel seismic (MCS) data along the
237 line. A basic processing sequence included bandpass filtering from 5-125 Hz, normal-move out
238 (NMO) based stacking, and migration with a constant velocity of 1.5 km/s, which provided
239 seismic images of the sediment cover and the depth of the igneous basement (Supplementary
240 material Fig. S4). Due to the large shot interval and consequently low fold, the quality of the
241 seismic image is poor below the basement. The MCS data were therefore mainly used to
242 constrain the depth and shape of the basement below the sediment cover. Thus, both seafloor and
243 basement were picked on the post-stack time-migrated section and converted to depth for the
244 tomographic travel time inversion using the acoustic velocity of water and a constant velocity for
245 sediments of 1.86 km/s derived as a mean from the semblance analysis of the ultra-long streamer
246 data (Marjanović et al., 2020). Additional constraints on the sedimentary blanket along IS-01 are
247 available for the coincident seismic profile of Mehouchi and Singh (2018).

248 3.3 OBS Processing

249 The OBS data were corrected for the internal clock drift and were relocated using the symmetry
250 of the direct wave and a least-squares method (e.g., Creager & Dorman, 1982). The acoustic
251 sound speed profile of water was obtained by onboard Expendable Bathythermograph (XBT) and
252 World Ocean Circulation Experiment (WOCE) Conductivity/Temperature/Depth (CTD) data.
253 The OBS depth was further corrected to match the constrained seafloor depth and a
254 corresponding time shift was applied to the travel times. In this study, we only use the pressure
255 components of the OBSs. The processing of the OBS data was carried out with Seismic Unix
256 (Cohen & Stockwell, 2010) using the same sequence and parameters for both lines. A
257 Butterworth-bandpass filter from 4-20 Hz was applied to the OBS gathers to filter low and high
258 frequency noise. Moreover, a predictive deconvolution was applied to suppress some energy of
259 the bubble reverberations and to facilitate the identification of the wide-angle reflection events.
260 The shape and length of the wavelet, which is crucial for the performance of the predictive
261 deconvolution, was obtained using a trace autocorrelation methodology (Yilmaz, 2001).

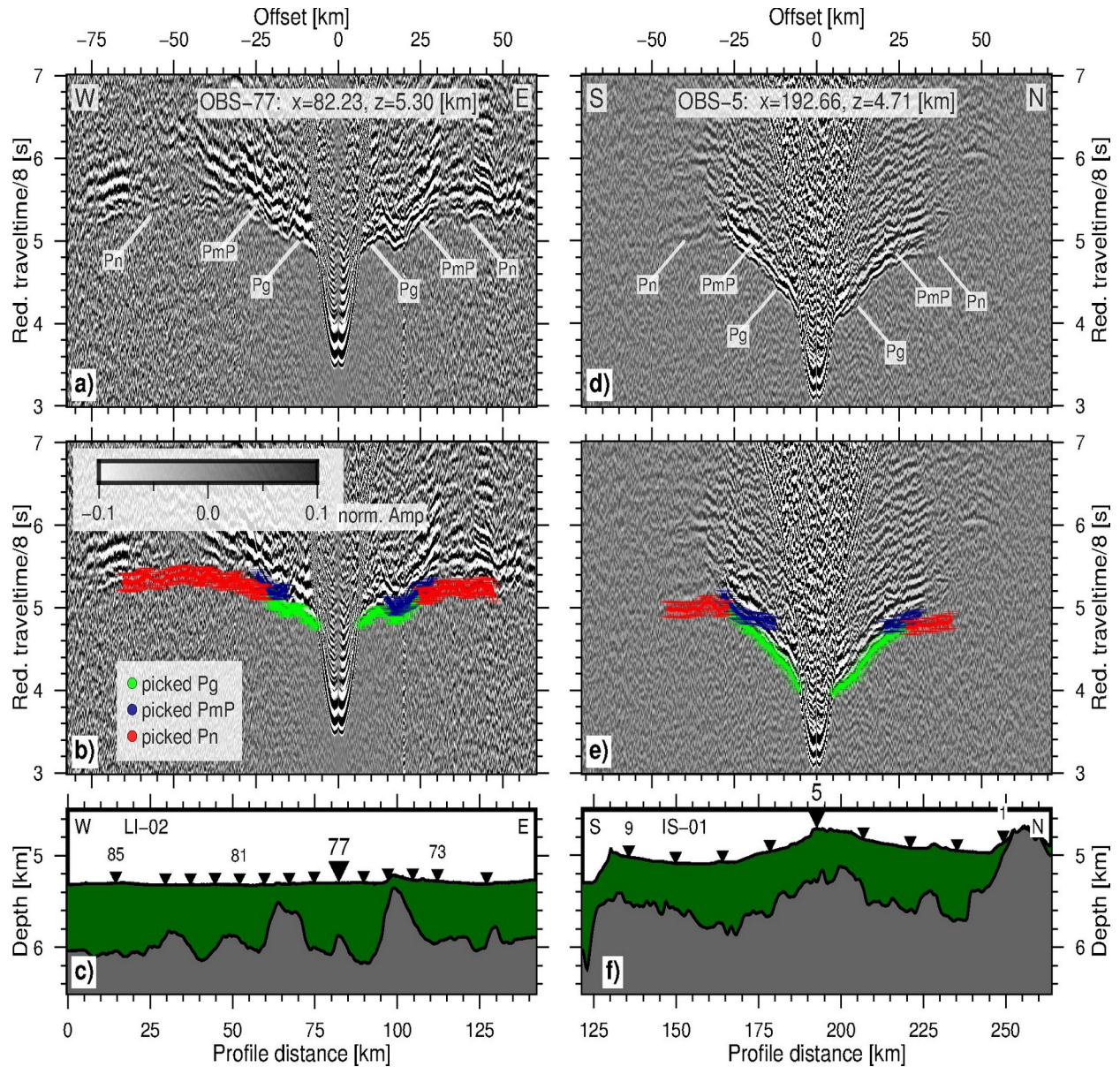


Figure 2: Record sections, labelled events and arrival picks for two selected OBS. **(a,d)** Processed receiver gathers of OBS 77 (panel a; LI-02) and OBS 5 (panel c; IS-01) with labelled seismic events. The travel time is reduced with 8 km/s. The amplitude is normalized by its maximum and clipped to 10 %. The X and Z coordinate represent the along-profile-axis distance and the water depth of the OBS. **(b,e)** The same record sections with travel time picks superimposed where colored dots and error bars illustrate the picked arrivals for the three distinct seismic phases (Pg, PmP, Pn; see legend) and their individual pick uncertainty. **(c,f)** Corresponding OBS locations (black inverse triangles), bathymetry and the sediment thickness (green area) above the igneous basement (gray area). The OBS of the illustrated receiver gather is highlighted. Every fourth OBS is labelled.

274 4 Tomographic Traveltime Inversion

275 For the tomographic inversion, a total of ~ 10100 refracted first arrivals (Pg and Pn) and ~ 2700
 276 wide-angle reflection arrivals (PmP) were manually picked on the 29 receiver gathers (along
 277 both lines) and an offset-dependent uncertainty was assigned to each pick (e.g., Fig. 2). The
 278 estimated uncertainties are 30-50 ms for Pg, 70 ms for PmP, and 80-110 ms for Pn arrivals. Both
 279 the forward modeling and inversion were carried out using the package TOMO2D from
 280 Korenaga et al. (2000). This code applies a hybrid scheme of the shortest path method from
 281 Moser (1991) for calculating the least traveltimes between the grid nodes followed by a ray
 282 bending method (Moser, 1992) to fine-tune these initial ray paths and minimize their travel
 283 times. The ray bending is thereby conducted using a conjugate gradient method (Moser, 1992).
 284 For the inverse problem the traveltime residuals for each raypath are equalized with
 285 perturbations of the velocity and the reflector nodes with respect to a reference model, forming a
 286 sparse linear system (Korenaga, 2000). Hereinafter, the linear system is normalized by data and
 287 model covariates, regularized with smoothing and damping constraints (Korenaga, 2000) and
 288 can be solved by the sparse matrix solver LSQR (Paige & Saunders, 1982).

289 The model domains were discretized into 726×141 (for line LI-02) and 1167×141 (for line IS-01)
 290 cells with a horizontal node spacing of 200 and 300 m, respectively. The larger horizontal node
 291 spacing for IS-01 was chosen due to the larger shot interval of 300 m. The variable vertical node
 292 spacing increases with depth from 50 m at the seafloor to 250 m at the bottom of the model.
 293 Initially, the horizontal and vertical correlation lengths, smoothing, and damping weights that
 294 regularize the nonlinear inversion were tested and evaluated. Since the seismic velocity generally
 295 varies more vertically than laterally, smaller vertical than horizontal correlation lengths were
 296 used, which increased linearly with depth. Based on the smaller shot and receiver spacing and
 297 hence the higher resolution, slightly smaller correlation lengths were used for the line LI-02.
 298 Additionally, considering the lower uncertainties of Pg picks, we chose smaller regulation
 299 weights for the Pg inversion than for the PmP and Pn inversion steps. A 1-D velocity model of
 300 oceanic crust hung below the constrained sediment/basement interface (Fig. 3) was used as a
 301 starting velocity model. All parameters of the discretization, forward modelling and inversion are
 302 also listed in Table S2 in the supplementary material.

The inversion was carried out following a top-to-bottom approach. Hence, first, the near offset Pg arrivals were inverted to constrain the shallower upper crust before adding the further offset Pg arrivals and inverting again to obtain the velocity structure of the upper and intermediate depths of the crust. Thereafter, the PmP reflection arrivals were added and inverted with an initial flat Moho reflector with a predefined constant depth (on average 6 km below the mean basement depth). The reflector is modeled as a floating reflector with only one degree of freedom vertically, and is thus independent from the velocity nodes (Korenaga et al., 2000). A depth kernel weighting factor, which controls the tradeoff between the velocity and the reflector depth ambiguity from the PmP arrivals (Korenaga et al., 2000) was chosen to be 1 such that velocity and reflector depth perturbation are equally weighted. Each iterative inversion stage in the top-to-bottom approach is stopped by reaching a normalized target $\chi^2 \leq 1.2$ or when a maximum number of iterations (eight for each Pg segment and PmP) is reached, which results in an excellent fit to observed and calculated travel times (Fig. 4). The ray coverage in the model domain is represented by the derivative weight sum (DWS; Toomey & Foulger, 1989), which incorporates not only the number of rays going through each cell but also their individual path length through the cell and their uncertainty.

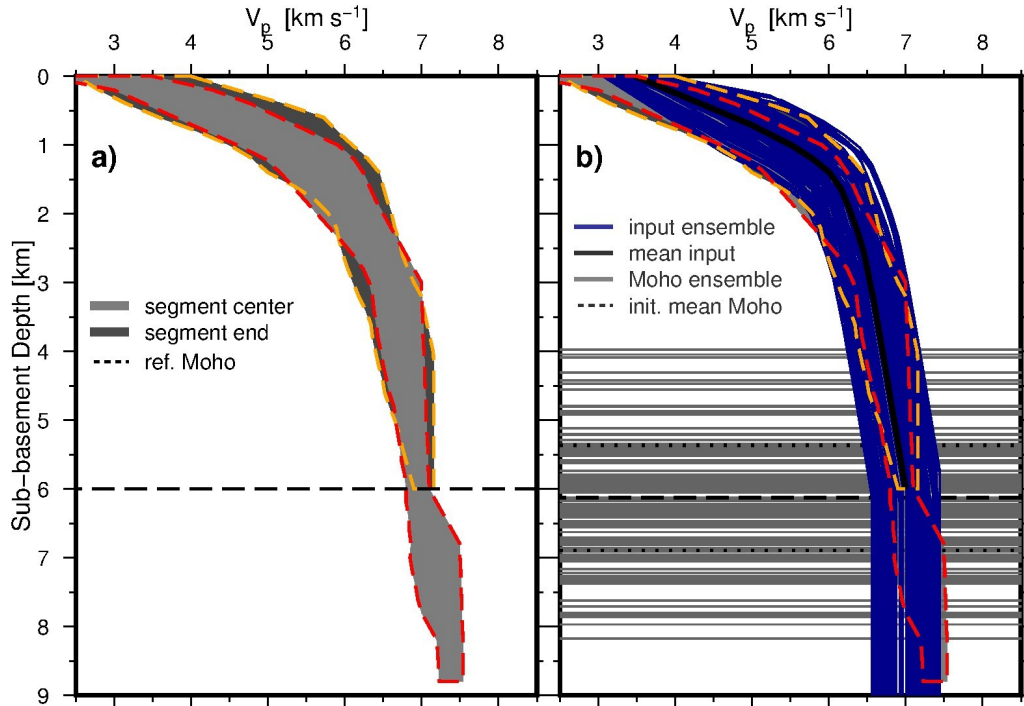


Figure 3: Velocity and Moho reflector input ensembles. **(a)** Reference velocity ensembles and crustal thickness obtained for the central portion of the MAR segments (light grey, dashed orange frame) and the segment ends (dark grey, dashed red frame) after Grevenmeyer et al. (2018). **(b)** Randomized input velocity (blue) and initial flat Moho (light grey) ensemble for Monte Carlo analysis. Solid, dashed, and dotted black lines indicate the mean initial 1D-velocity-depth function, the mean initial flat Moho and its standard deviation, respectively.

336 To minimize the bias from the initial model and to evaluate the model uncertainty, a Monte Carlo
337 analysis (MCA) was performed in which a set of 100 randomized starting velocity models (e.g.,
338 Fig. 3) and a set of 100 initial flat Moho reflectors of various constant depths were inverted and
339 averaged to obtain the final crustal model and its standard deviation (see Appendix 1). For the
340 MCA, the 100 1-D input velocity functions were randomized around a reference velocity
341 function for the Atlantic crust, which is derived as a mean from a compilation of velocity-depth
342 profiles from the Atlantic Ocean for ridge segment ends (Grevemeyer et al., 2018; Fig. 3). The
343 100 initial flat reflectors were randomized around a flat Moho reflector 6 km below the average
344 basement depth.

345 After obtaining the final average crustal velocity model from the MCA, an initial velocity model
346 for the upper mantle was added and hung below the mean constrained Moho reflector. To create
347 the initial 1-D input velocity function for the upper mantle, we observed an apparent velocity of
348 8 km/s in the Pn arrivals within the data, and reduced this slightly to 7.8 km/s at the Moho depth.
349 Below the Moho, the mantle velocity increase was defined subsequently by three velocity
350 gradients: 0.1 s⁻¹ from 0 to 1 km, 0.05 s⁻¹ from 1 to 5 km, and 0.04 s⁻¹ from 5 km to the model
351 bottom. In the final stage of the entire cumulative inversion scheme, the picked Pn arrivals were
352 added, and all arrivals were inverted to obtain the final result that included the velocity in the
353 crust, the Moho reflector, the uppermost mantle (Figs 5 and 6). Due to the high uncertainty of the
354 Pn picks (80-110 ms) and a previously well constrained final crustal model, a normalized $\chi^2 \leq 1.2$
355 was thereby reached after only 2-3 iterations, despite larger damping weights in order to avoid
356 significant changes within the already constrained crust. The model error is estimated by the
357 computation of the RMS-fit and the normalized χ^2 , which incorporates the data variance,
358 represented by the individual pick uncertainty.

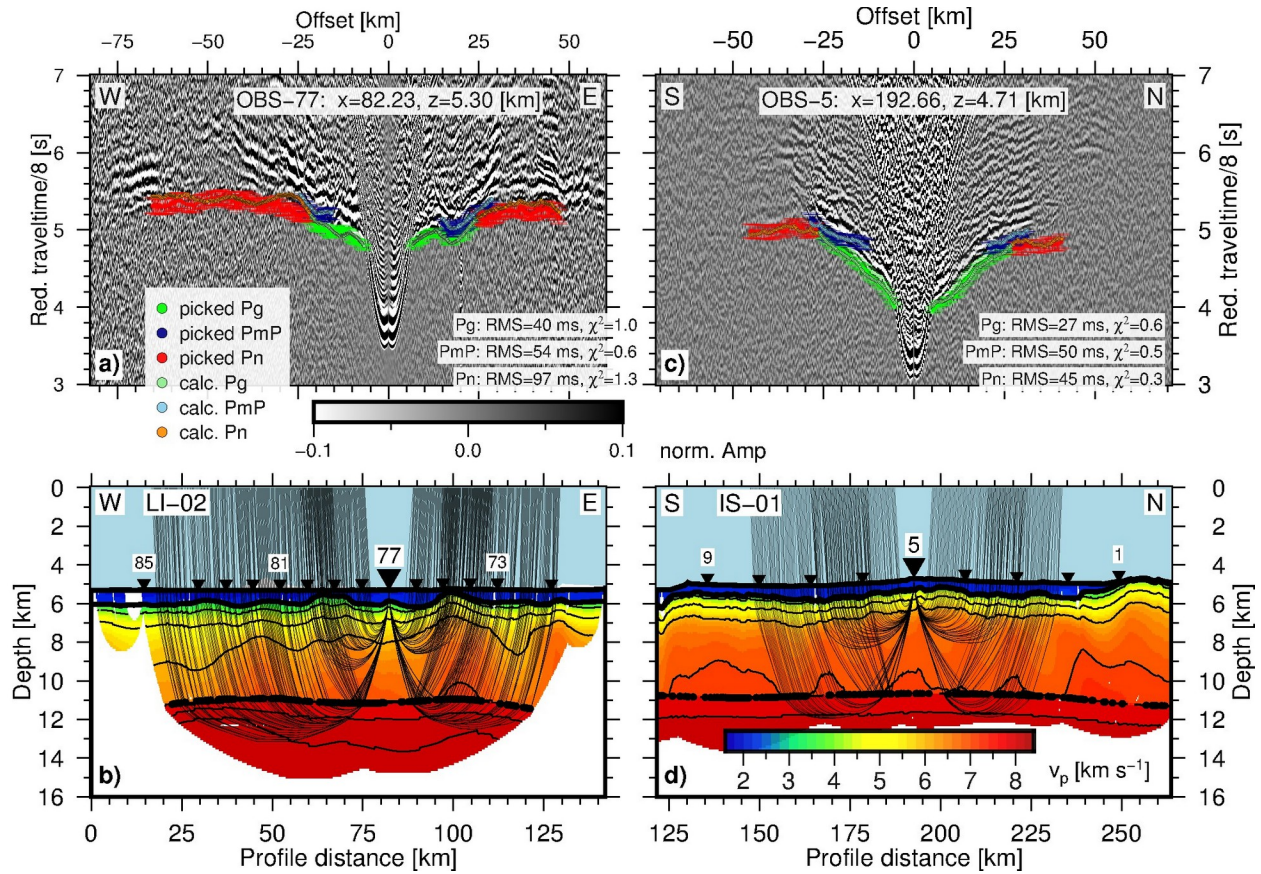


Figure 4: Traveltime fits and raypaths for two selected OBS. **(a,c)** Processed receiver gathers of OBS 77 (panel a) and OBS 5 (panel c) with picked and calculated travel times superimposed and **(b,d)** their corresponding ray paths superimposed on the final velocity models centered at OBS-5 (d) north of and OBS-77 (b) within the SPFZ-1. Thick black dots denote the modelled Moho reflection points, respectively. The velocity contour interval is 1.0 km/s for the crust, starting with 4 km/s, and 0.1 km/s for the mantle, starting at 8.0 km/s. The remaining elements are the same as in Figure 2.

To estimate the spatial resolution and the sensitivity of the inversion scheme with respect to the parametrization of the model space, we conducted multiple checkerboard tests with varying wavelengths and a velocity perturbation amplitude of 10 % (see Figs. S6 and S7 in the supplementary material). The results show that anomalies of 25 km horizontal and 5 km vertical diameter are well resolved with nearly full amplitude for both profiles. Anomalies of 15 km horizontal and 3 km vertical diameter are only fairly well resolved in the upper to intermediate crust. In particular, the low velocity anomalies are poorly recovered in the lower crust. We further tested the resolution of our method in terms of the combination of both an anomalous sinusoidal Moho reflector, with an oscillating perturbation amplitude of 1 km, and gaussian velocity anomalies with a perturbation amplitude of 10 %, placed above it in the lower crust. The results show a very good recovery of the velocity anomalies and a recovery of the anomalous reflector of ~60-70% (Figs. S8 and S9). Finally, to test the sensitivity within the mantle we introduced gaussian anomalies with a horizontal diameter of 50 km, a vertical diameter of 3 km and a perturbation amplitude of 5 % (Figs. S10 and S11) below the constrained Moho reflector. The results reveal that positive anomalies in the mantle are well resolved up to a perturbation amplitude of 0.2-0.3 km/s. Conversely, the negative anomalies are with amplitudes up to only 0.1 km/s significantly less recovered. All results of the resolution tests are included in the supplementary material.

5 Tomographic Results

In the following paragraphs the results of the tomographic travel time inversion are presented separately for the two seismic lines: LI-02 running along the St. Paul fracture zone (Fig. 5) and IS-01 crossing the St. Paul fracture zone. Note, the results of line IS-01 running north-south (Fig. 6) are subdivided into the distinct areas of north of the SPFZ-1, crossing the SPFZ-1 and south of the SPFZ-1.

5.1 LI-02: Along the St. Paul Fracture Zone

5.1.1 LI-02: Crustal Seismic Structure along the St. Paul Fracture Zone

The crustal thickness along LI-02 varies from $4.8\text{--}5.6\pm 0.3$ km, resulting in a mean crust of 5.2 km (Tab. 1 and Fig. 7b). The velocities along the FZ, particularly in the western and central part of the profile, are remarkably lower in the upper and mid-crust with respect to the reference model (0.2-0.7 km/s; Fig A1). Along most of the profile, the seismic velocities do not exceed 5 km/s within a sub-basement-depth of 1 km, and the usual seismic layer 3 velocity of ~6.6 km/s (e.g., Christeson et al., 2019; Grevemeyer et al., 2018) is reached not before 3-4 km depth into the crust (Figs 5 and 8). However, the eastern part of the profile shows slightly higher velocities of up to ± 0.2 km/s with respect to the reference model and $\pm 0.4\text{--}0.8$ km/s with respect to the western part of the profile. Further, these higher velocities (from 90 – 110 km along profile distance) coincide with a basement high within the FZ (Figs 5 and 7) and thicker crust, indicating an enhanced magma supply.

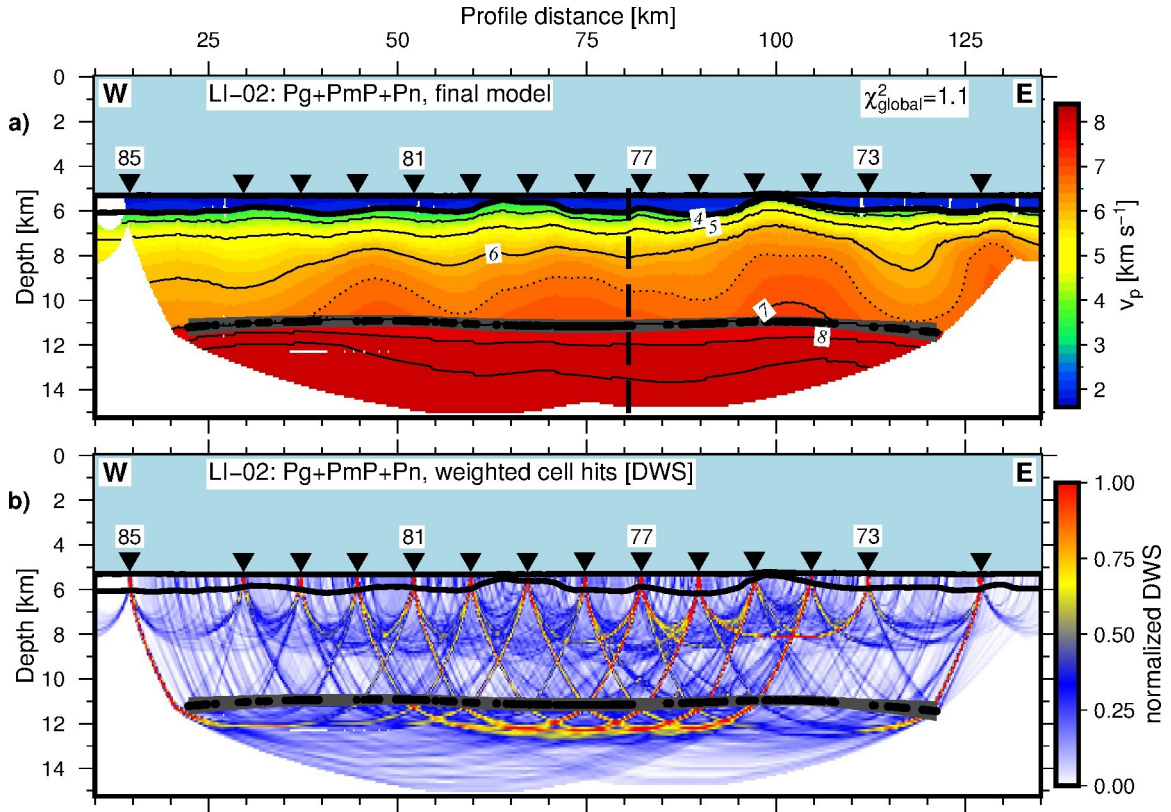


Figure 5: Inversion results for line LI-02. **(a)** Crustal and upper mantle velocity model obtained by cumulative Pg, PmP and Pn inversion. The contour interval is 1 km/s in the crust starting at 4 km/s and 0.1 km/s in the mantle starting at 8.0 km/s. The dotted line represents a usual velocity of the lower crust of 6.6 km/s. Black dots and grey shading denote the modelled Moho reflection points and the Moho standard deviation, respectively. The vertical dashed line depicts the intersection location with line IS-01 (Fig. 1b). The remaining elements and symbols are the same as in Figure 4. **(b)** Corresponding normalized DWS for the crust and upper mantle.

5.1.2 LI-02: Upper Mantle Structure along the St. Paul Fracture Zone

The Pn inversion yields a rather homogeneous upper mantle with velocities of ~8 km/s along the profile LI-02 and hence parallel to the spreading direction (Figs. 5 and 7). Abundant far offset Pn arrivals up to 100 km on several OBS gathers provide ray penetration up to 6 km below the Moho, and hence a good ray coverage in the upper mantle (Fig. 5). Therefore, these mantle velocities are real and not attributable to the initial velocity model.

5.1.3 LI-02: Uncertainties along the St. Paul Fracture Zone

The final computed Pg, PmP, and Pn arrivals yield RMS fits of 46, 56, and 91 ms, respectively, and result in a normalized global χ^2 of 1.1. During the MCA, the standard deviation of the velocity model is reduced from 0.3-0.5 km/s to <0.2 km/s in the upper crust and < 0.1 km/s in the intermediate and lower crust (Fig. A1). The standard deviation for the Moho reflector depth and hence the crustal thickness is reduced from an initial 0.75 km to a mean of 0.3 km. The mean values and uncertainties for both crustal thickness and velocities are provided in Table 1.

435 5.2 IS-01: Across the St. Paul Fracture Zone

436 5.2.1 IS-01: North of SPFZ-1

437 The final crustal model for IS-01 reveals a relatively constant crustal thickness along the whole
438 profile (Figs 6 and 7) but can be subdivided into the two parts: north and south of the SPFZ-1 in
439 terms of velocity structure. The part north of the FZ encompasses a distance of ~ 110 km (from
440 130 km to 240 km along profile distance), which displays a crustal thickness of $5.0\text{--}5.4\pm 0.3$ km
441 (mean= 5.3 km). A thick crust, $\sim 6.5\pm 0.5$ km (Fig. 7), is observed at the northern end of the profile
442 in a 15-20 km wide zone (at distance ~ 240 km), which coincides with a high basement
443 topography (Figs 6 and 7). However, since the Moho reflector north of ~ 240 km (along profile
444 distance) is not constrained by reversed ray coverage (Fig. 6), it may not be resolved properly
445 and is hence excluded from the further interpretation and statistical computations. The velocity
446 structure north of the FZ is relatively uniform and shows significantly higher crustal velocities
447 ($+0.2\text{--}0.6$ km/s) with respect to the reference model (Fig. A2).

448 The velocity depth-profiles in this region extracted from the final crustal velocity model (in
449 Figure 8 marked as o, p, and q) resemble the seismic structure of usual oceanic crust containing
450 the two-layer gradient structure with a high-velocity gradient in the upper crust and a low-
451 velocity gradient in the intermediate and lower crust representing mafic layer 2 and the gabbroic
452 layer 3, respectively (Fig. 8 b, c). Here, layer 2 reveals velocities ~ 4 km/s at the top increasing
453 to $\sim 6.2\text{--}6.5$ km/s at its base ($\sim 1.6\pm 0.3$ km sub-basement depth); the velocities of layer 3
454 increase from $\sim 6.5\text{--}6.7$ km/s at the top of the layer to $\sim 6.9\text{--}7.2$ km/s at the base of the crust.

455 When compared to most of the profiles from LI-02, along the FZ, the layer 2-layer 3 boundary is
456 more distinctively defined north of St. Paul. Further, crustal velocities are generally higher, with
457 values of $\sim 4.5\text{--}5$ km/s in the upper crust compared to <3.5 km/s at the top of the crust along the
458 FZ, and values of >6.8 km/s in the lower crust compared to $\sim 6.3\text{--}6.8$ km/s at the base of the crust
459 along the FZ. However, the eastern domain of LI-02 (profiles d, e in Fig. 8) shows a closer
460 similarity to the crust north of St. Paul, with a potential layer 2-layer 3 interface of transition
461 zone occurring at ~ 1.7 km below the basement.

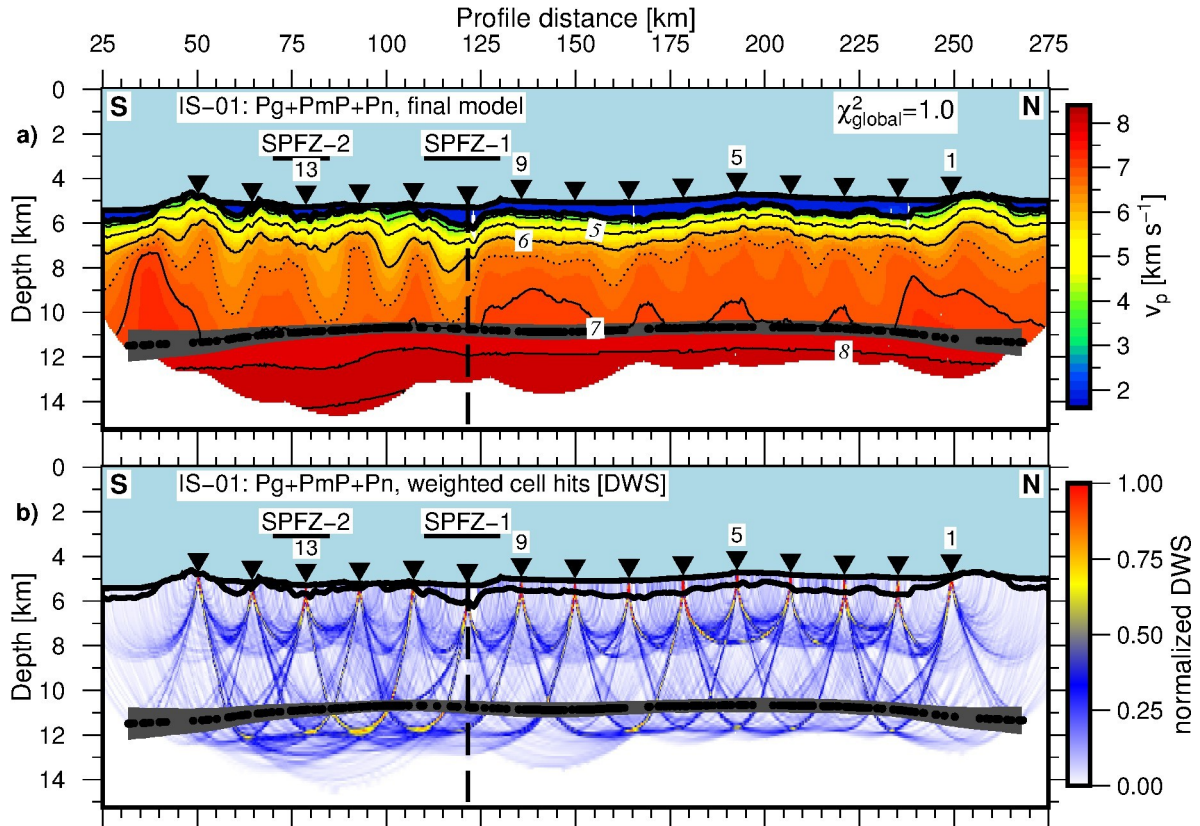


Figure 6: Inversion results for line IS-01. **(a)** Crustal and upper mantle velocity model obtained by cumulative Pg, PmP and Pn inversion. **(b)** Corresponding DWS for the crust and upper mantle. Thick horizontal labelled bars indicate the two FZs and their extent derived from the bathymetry (Fig. 1b). The remaining figure elements and contour intervals are the same as in Figure 5.

5.2.2 IS-01: Across SPFZ-1

Across the SPFZ-1 from north to south, the crustal thickness decreases from 5.2 ± 0.3 km to 4.8 ± 0.3 km (Figs 6 and 7). Within a distance of ~ 20 km from the center of the valley, the crust thickens again to 5.3 ± 0.4 km, resulting in a zone of reduced crustal thickness about 20 km-wide. The FZ exhibits only slightly lower velocities compared to the reference model at segment ends (Fig. A2). However, with respect to the adjacent crust in the north of the FZ it reveals a remarkable velocity reduction of 0.4–0.8 km/s throughout the upper and mid-crustal region (Fig. 8c: compare profile n with o, p, q).

475 5.2.3 IS-01: South of SPFZ-1

476 The southern part of the profile differs remarkably from the observations in the northern part,
 477 showing more heterogeneities both in crustal thickness and velocities (Figs 6 and 7). The crust
 478 thickens from the FZ southwards from a rather thin crust of 4.8 ± 0.3 km to 5.6 ± 0.3 km within a
 479 distance of ~ 60 km (from 115 km to 55 km along reverse profile distance) and reaches a
 480 maximum thickness of 6.7 ± 0.4 km below another basement high at the southern end of the
 481 profile. However, similarly to the northern limit of the profile, the crustal thickness for distance
 482 < 55 km is not very well constrained and hence is not included in the statistical computations and
 483 discussion. The velocity distribution shows both positive and negative anomalies with respect to
 484 the reference model, but the velocities are generally lower than those north of the FZ by 0.2–0.8
 485 km/s (Figs 8 and A2). The strong velocity variations affect both the upper and the lower crust.
 486 Parts of the structure south of St. Paul, for example, the low velocity zone just north of the
 487 SPFZ-2 (profile m in Fig. 8a, c), show a similar range of velocities to the structure along the FZ.
 488 However, they also show a clear division into two layers with a high gradient upper crust and
 489 low gradient mid- to lower-crust (occurring at ~ 1.5 km for profile m), and so cannot be
 490 considered to exhibit the same crustal structure as inside the FZ. Conversely, other sections south
 491 of St. Paul, such as at ~ 70 km along profile (profile l in Fig. 8a,c), show a more similar velocity
 492 structure to the crust north of the FZ.

493 5.2.4 IS-01: Upper Mantle Structure across SPFZ

494 The Pn inversion yields rather homogeneous upper mantle velocities of 7.8–8 km/s along the
 495 whole profile IS-01 (Figs 6 and 7). Due to a decreasing signal/noise ratio at far offsets in some
 496 record sections and a conservative picking approach of only including picks with uncertainties of
 497 < 0.12 s, Pn offsets of good quality were generally limited to offsets smaller than 60 km.

498 5.2.5 IS-01: Uncertainties across SPFZ

499 The final computed Pg, PmP, and Pn arrivals yield RMS fits of 41, 67, and 85 ms, respectively,
 500 resulting in a global normalized $\chi^2 = 1.0$ for both the crustal and the joint crustal and mantle
 501 models. An example of traveltimes fits is illustrated in Figure 4. During the MCA, the velocity
 502 standard deviation was reduced from 0.3–0.5 km/s to ~ 0.2 km/s in the upper crust and < 0.1
 503 km/s in the middle and lower crust (Fig. A2). The significantly higher uncertainty in the shallow
 504 crust is caused by predominantly vertical travel path of the rays and the resulting low sensitivity.
 505 The ray coverage is highest between 1.5–2.0 km of sub-basement depth since this is the depth
 506 where the most rays turn (Fig. 6). Note that beyond the receiver line the crustal velocities are
 507 constrained by only one-sided ray coverage and thus yield a very high uncertainty. The standard
 508 deviation for the Moho reflector depth and hence the crustal thickness north of the FZ, the FZ
 509 itself and south of the FZ is reduced from 0.75 km to 0.3 km. Mean values and uncertainties for
 510 both crustal thickness and velocities are provided in Table 1.

511 5.3 Summary of Results

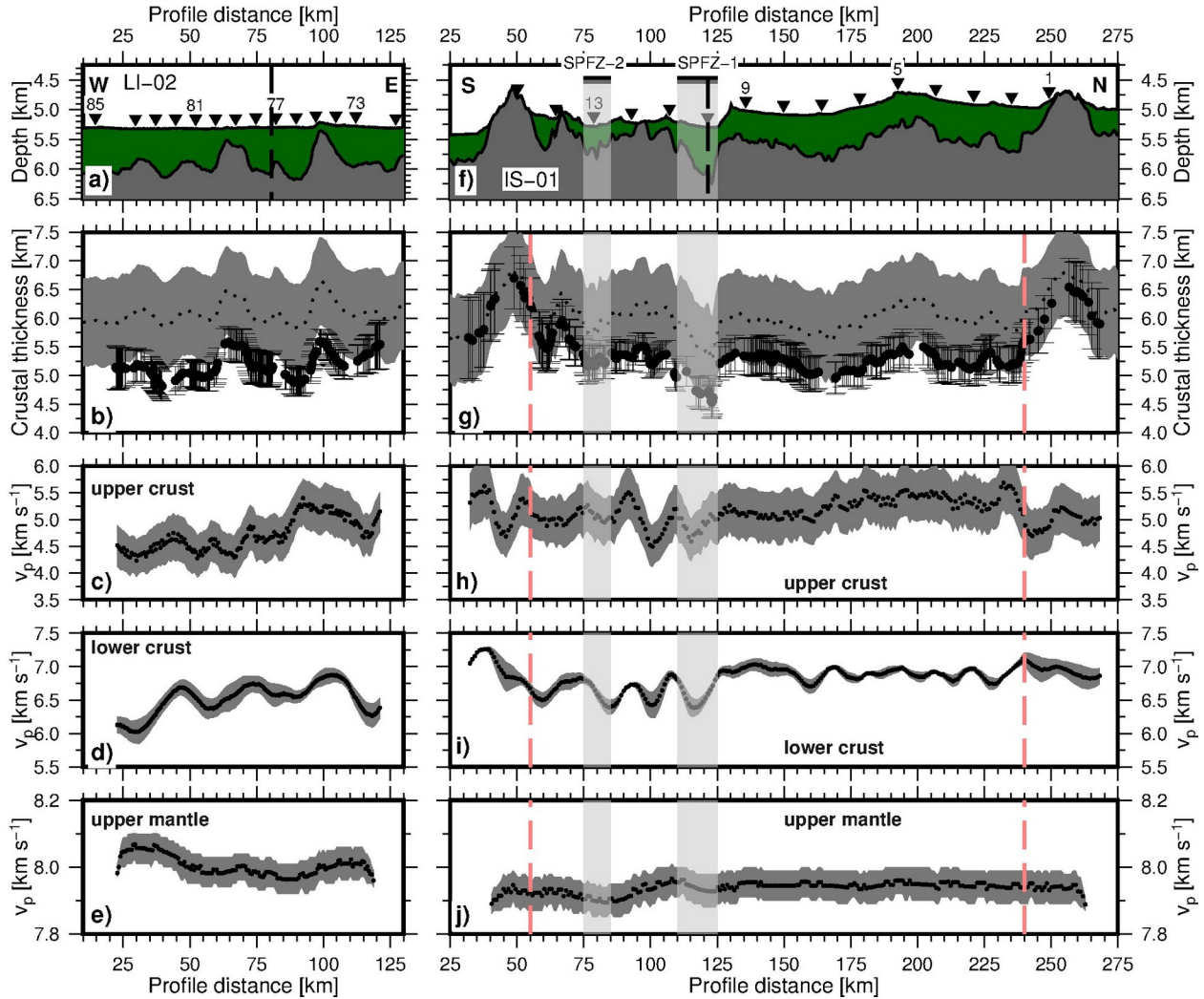


Figure 7: Bathymetry, sediment and crustal thickness as well as mean velocities for upper and lower crust and upper mantle along both refraction lines (LI-02: panels a-e, IS-01: panels f-j). **(a,f)** Bathymetry, sediment thickness (green region) above the basement (gray region) and OBS locations. **(b,g)** Black dots with error bars denote the crustal thickness obtained from the modelled Moho reflection points and their standard deviation. The dotted line and grey shading denote the mean and standard deviation of the crustal thickness input ensemble. **(c-e, h-j)** Vertically averaged velocities for the upper crust (panels c,h; 0.25 - 1.25 km sub-basement), lower crust (panels d,i; 0.25 - 2.5 km above Moho) and the upper mantle (panels e,j; 0.25 - 1.25 km below Moho) and their corresponding standard deviation (grey shading) along the two lines, respectively. Vertical light grey shading indicates the extent of the two fracture zone valleys (SPFZ-1, SPFZ-2; Fig. 1). Vertical red dashed line excludes the edge regions that are not constrained by reverse ray coverage for IS-01. Remaining elements are the same as in Figure 2 and 5.

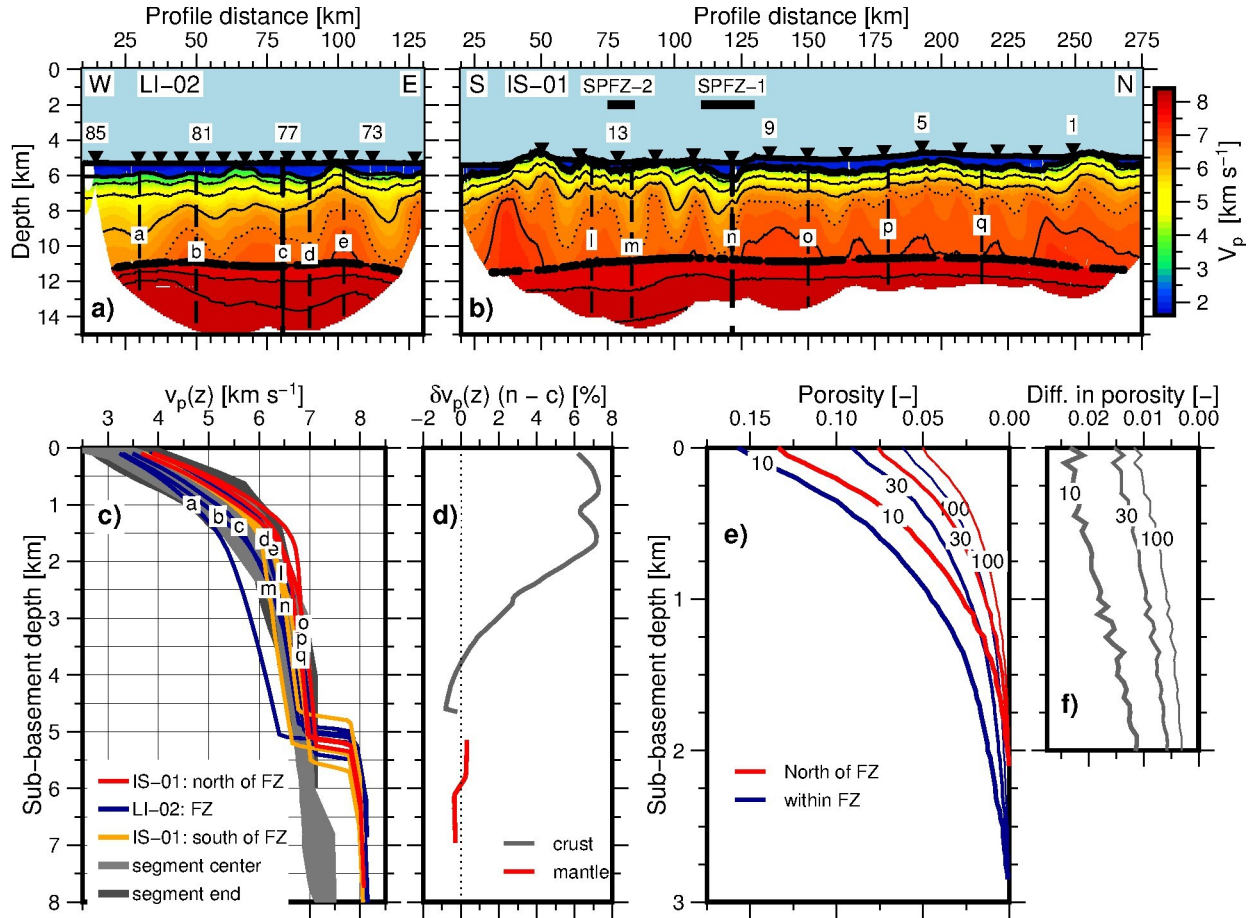


Figure 8: Velocity and porosity compilation for the two lines. (a,b) The locations for the selected 1-D velocity-depth profiles (labelled vertical dashed lines) of line LI-02 (a) and line IS-01 (b) are superimposed on the final velocity models. Remaining figure elements are the same as in Figure 5. (c) Extracted velocity depth profiles. Each profile represents the average of the velocity-depth profiles for four adjacent horizontal nodes. (d) Velocity difference within the vicinity of the profile intersection (profile n – profile c). (e) Porosity estimates using DEM analysis for averaged velocity depth functions of the SPFZ-1 (averaged from 15 -120 km distance alongside LI-02) and the crust north of it (averaged from 130 -240 km distance alongside IS-01). The labels indicate different aspect ratios of the fractures. (f) Difference in porosity between the crust within the fracture zone and north of it (FZ – North).

Table 1 lists the findings of this study regarding crustal and upper mantle properties for three distinct regions: north of St. Paul, south of St. Paul, and along the St. Paul FZ itself. The mean upper crustal velocity is obtained from averaging vertically and horizontally down from 0.25-1.25 km of sub-basement depth. The lower crustal velocity is obtained by vertical and horizontal averaging of the 0.25–2.5 km (reversed depth) of the lower crust just above the constrained Moho reflector. The mean upper mantle velocity is obtained from vertical and horizontal averaging between 0.5-2 km below the constrained Moho reflector. Only regions with sufficient ray coverage contribute to these statistical computations. The overall variability of the velocity structure in the survey area is also summarized in Figure 9, where 1-D velocity depth profiles are extracted for both lines with an interval of three horizontal nodes and colored for the distinct regions.

545 Table 1: Summary of the main findings regarding crustal and upper mantle properties.

Parameter / Location	North of FZ	Along FZ	South of FZ
Crustal thickness [km]	5.3 ± 0.3	5.2 ± 0.3	5.4 ± 0.3
Vp upper crust [km/s]	5.2 ± 0.5	4.7 ± 0.4	5.1 ± 0.4
Vp lower crust [km/s]	6.9 ± 0.1	6.5 ± 0.1	6.7 ± 0.1
Vp upper mantle [km/s]	7.9 ± 0.05	8.0 ± 0.05	7.9 ± 0.05

546
547

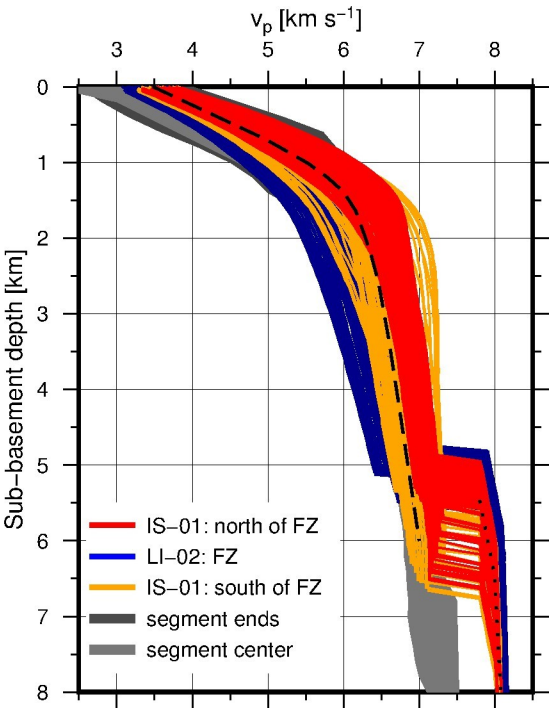


Figure 9: Velocity-depth compilation. The 1-D velocity-depth functions are extracted with an interval of three horizontal nodes (0.6 km for LI-02 and 0.9 km for IS-01, respectively) and color coded for the distinct regions (see legend). Grey shading indicates the reference velocity ensemble from Grevenmeyer et al. (2018). The dashed and dotted lines denote the mean initial velocity-depth function for the crust and the initial velocity-depth function used below the constrained Moho for the Pn inversion, respectively.

6 Discussion

6.1 Crustal Thickness along the St. Paul Fracture Zone

In the literature the term fracture zone has been loosely used for both the tectonically and seismically active transform fault offsetting the spreading axis and its inactive fracture zone (e.g., Detrick et al., 1993). Here, we will use the term “transform fault” for the active plate boundary offsetting the spreading axis, while with the term “fracture zone”, we will refer to the inactive fossil trace where lithosphere of contrasting age meets and subsidence occurs on either side depending upon their thermal structures (e.g., Menard, 1967; Sandwell, 1984). This clear separation between the fracture zones and the transform faults are important as recent evidence suggest that crust accreted along a transform fault might be affected by processes acting at ridge-transform intersections before it converts into a fracture zone (e.g., Grevenmeyer et al., 2021; Marjanović et al., 2020).

The St. Paul fracture zone reveals an average crustal thickness of ~ 5.2 km, which is roughly 1 km thinner when compared to the global average of normal oceanic crust of 6.15 km thickness (e.g., Christeson et al., 2019), but close to the thickness of oceanic crust in the equatorial Atlantic, from $5.6\text{--}6.0 \pm 0.1$ km (Vaddineni et al., 2021). Interestingly, it did not show any significant change in the crustal thickness with respect to the crust found either to the north or south of the FZ. Furthermore, its thickness is in the same order of magnitude as the Chain FZ (Marjanović et al., 2020) and falls in the range of other FZ surveyed in the Atlantic Ocean, e.g. ~ 4.5 km at Tydeman FZ (e.g., Calvert & Potts, 1985; Potts et al., 1986a), ~ 5 km for the Mercurius FZ (Peirce et al., 2019). Additionally, Davy et al. (2020) observed a crustal thickness of ~ 6 km for the Late Cretaceous Marathon FZ. A new compilation of crustal thicknesses of major Atlantic TF and FZ (Marjanović et al., 2020) indicates thin crust at some transform faults (2-5 km) whereas most fracture zones have crustal thicknesses in the range of usual oceanic crust (5-7 km). An exception, however, is the Kane FZ, which shows a significantly thinner crust (2-3 km) (Cormier et al., 1984; Detrick & Purdy, 1980).

In general, the thinner crust found along transform faults and fracture zones is clearly consistent with the concept of focused mantle upwelling along mid-ocean ridges (e.g., Lin et al., 1990; Tolstoy et al., 1993), supporting magmatically starved conditions acting at transform faults. Further, geological observations and sampling of rocks from transform valleys at slow- and ultraslow-spreading ridges often reveals exposed upper mantle rocks near segment ends (e.g., Cannat, 1993; Cannat et al., 1995). These observations are consistent with the inferences from Detrick et al. (1993), suggesting that crust found at both transform faults and fracture zones is “thin, intensely fractured, and hydrothermally altered basaltic section overlying ultramafics that are extensively serpentinized in places”. However, the crust within the St. Paul FZ is only slightly (0.1-0.3 km) thinner when compared to oceanic crust adjacent to the FZ. A gradual crustal thinning over a distance of several tens of kilometers on either side of a fracture zone or transform fault, as reported previously for some fracture zones in the North Atlantic (White et al., 1984), is not observed, neither across the St. Paul FZ as shown in our data nor across the Chain FZ (Marjanović et al., 2020). One interpretation might be that the crust found along transform faults may deviate significantly from oceanic crust in fracture zones, as envisioned recently (Grevemeyer et al., 2021).

A similar deduction has been made recently to explain the crustal structure across the Chain FZ. Marjanović et al. (2020) suggested that lateral dyke propagation along the adjacent spreading axis into the transform fault augments crust at RTIs. Such a dyke injection is supported by the presence of J-shaped ridges in the vicinity of RTIs observed in a global study of transform faults (Grevemeyer et al., 2021). Bathymetric data obtained along the St. Paul FZ reveal a number of such J-shaped ridges, though ridge tips are often blanketed by sediments (Fig. 1c). Dyking is possibly controlled by 3-D mantle upwelling as envisioned by Lin et al. (1990) at slow spreading ridges. At the 21°30'N segment of the MAR, ridge propagation forced by lateral dyking has not only advanced into the transform domain, but cut through a transform fault, causing its die-off (Dannowski et al., 2018). We therefore propose that a second phase of RTI magmatic accretion might be an important process shaping the crust and lithosphere at the proximal end of transform faults. However, the proposed model is still rather conceptual and thus we cannot rule out that magma migrates also along the base of crust. A scenario where magma is supplied within the mantle before intruding into the crust may explain better the layer-2/layer-3 type layered structure of the crust found along St. Paul than a model where dyking along is governing RTI magmatism.

The occurrence of a second phase of RTI magmatism is supported by geological sampling, revealing that lithosphere along transform valleys is generally characterized by mantle exhumation (e.g., Fox et al., 1986; Tucholke & Lin, 1994), while outside corners and fracture zones are dominated by magmatically accreted basaltic crust (e.g., Karson & Dick, 1984). The observation that even the floor of a fracture zone valley (Karson & Dick, 1983) is composed of basaltic rocks supports the interpretation that transform crust is being augmented at RTIs by magmatism.

6.2 Seismic Velocity Structure along St. Paul Fracture Zone

Crustal seismic velocities along the SPFZ reveal significantly reduced values when compared to the crust north of the FZ. Throughout the upper and middle crust, velocities are reduced by 0.2-1.1 km/s. The velocity structure within the FZ, however, still shows the typical features of a two-layered crustal structure of normal oceanic crust of oceanic crust formed at segment ends (Fig. 8c), i.e., a high-velocity gradient upper crust and a low-velocity gradient lower crust. This decrease in seismic velocity throughout the entire crust might be best explained by the presence of large-scale porosity and fracturing of crustal rocks. Nevertheless, the observed layered structure closely resembling oceanic crust supports that crust, though fractured, was magmatically accreted. Therefore, the crust found along St. Paul FZ differs profoundly from the conventional wisdom where crust at discontinuities is generally characterized by basically a single layer and thin crust (e.g. Davy et al., 2020). For a mature oceanic crust near 15°N/55°30'W in the Atlantic Ocean, Davy et al. (2020) suggest that the structure of ridge crest discontinuities is controlled by the behavior of adjacent spreading segments. Therefore, crust accreted at discontinuities near magmatically starved spreading segments will mimic those conditions, while crust formed at transforms or higher-order ridge offsets adjacent to magmatically robust segments will reflect magmatically accreted crust. The accretion near St. Paul seems to have occurred during a period of constant magma supply from the mantle.

In order to estimate the porosities associated with decreasing velocity, we carried out a differential effective medium analysis (DEMA) after Taylor and Singh (2002). The DEMA was performed for a host rock of basaltic composition and assuming a population of aligned, elongate, fluid-filled fractures with aspect ratios (ARs) between 10 and 100 (Supplementary Fig. S5). The porosities are computed for laterally averaged 1-D velocity-depth profiles for both within the SPFZ-1 (line LI-02, from 25- 120 km along profile distance) and the crust resembling normal oceanic crust north of the SPFZ-1 (line IS-01, from 130-240 km along profile distance). The results and their deviation for three different ARs (10, 30, 100) are illustrated in Figures 8e and 8f. We obtain porosities decreasing from up to ~15% in the top of the crust to ~0 % at sub-basement depths at 2.0-2.75 km for an AR of 10. For an AR of 100 in contrast, the porosity is reduced from only ~6 % at the top of the basement to ~0 % at depths of 1.5-2 km. Depending on the AR the DEMA reveals porosities that are ~2.25 % (AR=10) to 0.5-1 % (AR=100) higher for the FZ with respect to the crust north of it (Fig. 8f). A recent study of the crust at the Romanche TF indicate that the porosity could be 15% near the seafloor decreasing to 1% at the base of the crust (Gregory et al., 2021). If similar porosity was present within the active St. Paul TF, the reduced porosity could be explained by combination of lateral dyke injection at the RTI (Marjanović et al., 2020) and hydrothermal alteration and mineral precipitation (Audhkhasi & Singh, 2019; Grevemeyer et al., 1999) during the early development of the fracture zone.

Increased porosity, which in turn causes decreasing seismic velocities, might be related to past deformation along the shear zone of the transform fault and/or emplacement of crust in a tectonically dominated environment at RTIs. This observation nurtures previous interpretation that fracture zones might be formed by hydrothermally altered basaltic and gabbroic sections that are to some degree fractured and faulted, as envisioned earlier (e.g., Detrick et al., 1993; White et al., 1984). However, even though crust might be partially altered and fractured, within the St. Paul FZ the mantle rocks do not seem to consist of extensively serpentinized peridotite. Instead, the presence of clear PmP reflection arrivals along the FZ valley and a continuous upper mantle Pn refraction with apparent velocity of ~ 8 km/s support a relatively dry mantle with a low degree of hydration or even the absence of upper mantle serpentinization along the entire section of the SPFZ-1. Inverted velocities along LI-02 are in the order of ~ 8 km/s (Fig. 7) and therefore much faster than mantle velocity of <7.5 - 7.8 km/s reported for some Atlantic transform faults (e.g., Detrick et al., 1993; Davy et al. 2020), supporting our interpretation. The dehydration of the mantle might be caused by the presence of higher temperature and crustal thickening dyke injection at the RTI, where the transform fault becomes a fracture zone.

6.3 Crustal Thickness as a Function of Distance across St. Paul Fracture Zone

Most previous studies along the axis of the MAR have revealed a strong dependence of crustal thickness variations along the ridge crest (e.g., Lin et al., 1990) and hence distance to a transform fault. For example, between 33 - 35°N of the MAR, Canales et al. (2000), and Hooft et al. (2000) observed that crustal thickness varies significantly as a function of distance from both the Oceanographer transform fault and non-transform offsets, showing thick crust at segment centers (up to 8 km) and thin crust at segments' ends (<3 km). Similar features are observed at the MAR at 21°N (Dannowski et al., 2011), and 5°S (Planert et al., 2009) and along the ultra-slow spreading Southwest Indian Ridge at 50°E (Niu et al., 2015), and 66°E (Muller et al., 1999). In general, crustal thickness at segment ends of slow-spreading ridges is in the order of 4-6 km thick and at segment centers thickness may increase to 7-9 km (e.g., Grevemeyer et al., 2018). It is, therefore, remarkable that our north-south profile reveals an almost constant thickness of 5.2-5.6 km over 100 km from the FZ with no obvious dependence of crustal thickness with distance to the St. Paul fracture zone at 2°N . Similar features are reported for the MAR in the vicinity of the Chain fracture zone, where crustal thickness is in the order of 4.6 to 5.9 km, showing no significant imprint of the transform discontinuity on ridge crest segmentation (Marjanović et al., 2020).

Another interesting feature is that the observed crustal thickness averages ~ 5.4 km along the ~ 200 km long north-south trending profile (IS-01). Farther south, between 0° and $\sim 3^\circ\text{S}$ around the Chain FZ, crustal thickness is 4.6-5.9 km (Marjanović et al., 2020) and at 2°S of the MAR the crustal thickness ranges from 5.6 to 6.0 km along a 600 km long flow line profile (Vaddineni et al., 2021). However, Christeson et al. (2020) reported from five ridge parallel profiles at 31°S a significant crustal thickness variations of 3.6 to 7.0 km for different crustal ages (6-60 Ma), but an almost constant thickness along each profile and thus for crust of the same age, suggesting that the equatorial and south Atlantic shows consistently thinner crust when compared to the average thickness of 7 km reported by White et al. (1992) for the Atlantic. However, we have to note that that data compiled by White et al. (1992) occurred predominantly in the North Atlantic with a large number of experiments in the north-western Atlantic where crust is in the order of 7-8 km (e.g., Purdy, 1983; Minshull et al., 1991), suggesting that previous estimates might be biased. In contrast, the majority of crustal thickness estimates, either along our profiles or elsewhere in the equatorial or south Atlantic region, compares well with global estimates of the global mean crustal thickness (e.g., Chen, 1992; Christeson et al., 2019; Harding et al., 2017; Van Avendonk et al., 2017), revealing an average global crustal thickness of 6.15 km (Christeson et al., 2019). Therefore, most observed crustal thickness estimates compare well to predictions from petrological models, suggesting an average crustal thickness of 6 km emplaced at a normal mantle temperature of 1300°C (e.g., McKenzie & Bickle, 1988; Korenaga et al., 2002). However, slightly reduced crustal thickness in the equatorial Atlantic of ~ 5.3 km between Chain and Romanche, roughly 6 km north of Romanche (Gregory et al., 2021) and <5.5 km along our longitudinal profile may supports a cooler mantle underlying the equatorial Atlantic. This interpretation is supported by the exceptionally low degree of melting of the upper mantle in the equatorial Atlantic as indicated by the chemical composition of mantle-derived mid-ocean ridge peridotites and basalts (Bonatti et al., 1993; Dalton et al., 2014) and upper mantle S-wave velocity (Grevemeyer, 2020; James et al., 2014).

6.4 Anisotropy

To assess the crustal and mantle anisotropy, the velocity structure from both seismic lines was compared in the vicinity of their intersection, averaging properties over a roughly 1 km long section (due to different node spacing we averaged 0.8 km along LI-02 and 1.2 km along IS-01). Figure 8d shows the velocity structure of the profiles at the intersection. Positive values indicate faster velocities mapped along line IS-01 running roughly north-south and hence parallel to the strike of the ridge axis. Anisotropy reaches a maximum of $\sim 7\%$ in the upper 2 km of the crust and decreases continuously to zero at a depth of ~ 4 km below the basement and thus may occur within the sheeted dykes. Within the upper mantle, no significant velocity anisotropy can be observed.

Our observation of the upper to mid-crustal anisotropy indicates higher velocities perpendicular to the fracture zone (i.e., along the strike of the ridge) with respect to velocities obtained parallel to the fracture zone (i.e., perpendicular to the ridge axis). It is interesting to note that our observations are consistent with that at the East Pacific Rise, where 4% of anisotropy was observed with the fast direction roughly trending along the strike of the ridge crest (e.g., Dunn & Toomey, 2001), which was interpreted to represent the effect of ridge-parallel trending faults. At St. Paul, the fast-direction seems also to be orientated parallel to the spreading axis. Therefore, if the observed crustal anisotropy would be caused by a set of faults it would support a set of faults cutting through FZ. Alternatively, anisotropy could be related to the emplacement of dykes, which are the dominant feature at 1 to 3 km depth in oceanic crust. One interpretation might therefore be that crustal anisotropy reflects J-shaped ridges migrating into the transform domain. However, one has to be careful in interpreting the crustal anisotropy as it is derived from two crossing profiles.

Another interesting feature is the lack of any apparent upper mantle anisotropy. Gaherty et al. (2004) observed 3.4% of upper mantle anisotropy in the North Atlantic to the south of Bermuda and in the Pacific mantle anisotropy is a striking feature, with values reaching 6-7% in short offset experiments at the East Pacific Rise (Dunn & Toomey, 1997; Dunn et al., 2000). Therefore, the absence of any anisotropy is a puzzling feature and it might therefore be reasonably to argue that mantle velocity along the fast direction and hence along the fracture zone might be with 7.9-8.1 km/s rather low. However, as stresses rotate over a short distance when approaching a transform fault (Morgan & Parmentier, 1984), mantle flow might be distorted along fracture zones and hence anisotropic pattern. In general, a velocity of ~8 km/s is in the range of observations from mature lithosphere when being sampled along ridge parallel profile (e.g., Davy et al., 2020; Gaherty et al. 2004) and much lower when compared to, for example, a flow line profile at 2°S where Vaddineni et al. (2021) observed in 20 to 30 Myr old lithosphere an upper mantle velocity of ~8.2 km/s. Observations obtained from the travel times of Pn arrivals of regional earthquakes recorded at moored hydrophones support this discrepancy, revealing for equatorial upper mantle a seismic velocity of 7.7 km/s in the slow and 8.4 km/s in the fast direction (de Melo et al., 2020). Therefore, it might be reasonably to suggest that some small degree of uppermost hydration along SPFZ might be hidden by effects of mantle anisotropy.

7 Conclusions

We presented new constraints from seismic reflection and wide-angle data surveying the crustal and upper mantle structure along and across the St. Paul fracture zone, one of the largest transform faults in the equatorial Atlantic Ocean. High-resolution P-wave travel time tomography revealed a number of key observations:

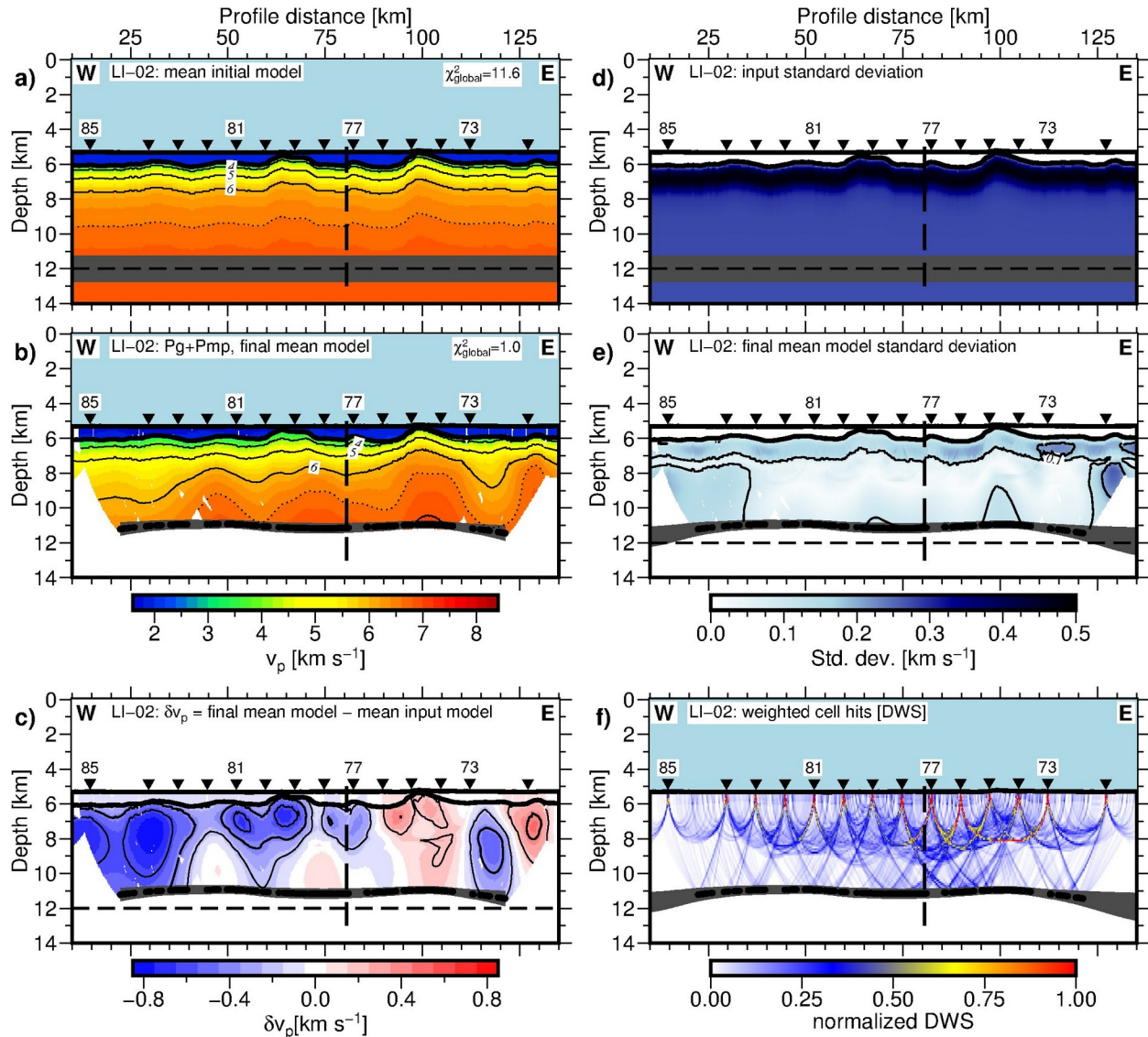
- 1.) Crustal structure along the fracture zone shows the typical layering of magmatically accreted oceanic crust with a crustal thickness of 5 to 5.5 km, a clearly defined seismic Moho and an upper mantle velocity of ~8 km/s.

2.) Crustal thickness across the fracture zone is in the order of 5 to 6 km, showing only a few hundreds of meters of crustal thinning in the vicinity of the St. Paul fracture zone. However, crust at St. Paul is slightly thinner than anywhere else along the line. Nevertheless, the roughly 200 km long well-resolved part of the fracture zone crossing profile did not show the same features and strong crustal thickness variation of 2-4 km found along the active Mid-Atlantic Ridge elsewhere (e.g., Canales et al., 2000; Dannowski et al., 2011; Hooft et al., 2000; Planert et al., 2009) and thus did not show strong evidence supporting decreased melt production and hence occurrence of magmatically starved crust at transform faults (e.g., Lin et al., 1990; Tolstoy et al., 1993).

3.) Crustal seismic velocities along St. Paul are a few percent slower than farther away from it. This observation may suggest that crust along the fracture zone has either higher porosity, probably caused by a larger degree of fracturing, or it may reflect anisotropy. Unfortunately, anisotropy is poorly resolved in the two crossing profiles.

4.) Mantle velocity of ~8 km/s along the transform fault did not reveal strong evidence for serpentinization of the uppermost mantle below the FZ, a feature which has previously been reported for a number of Atlantic fracture zones (e.g., Detrick et al., 1993) and was interpreted in terms of highly fracture and hydrated lithosphere. However, with ~8 km/s upper mantle velocity it is only slightly faster along the transform fault than with ~7.95 km/s across it, hardly showing any evidence for a strong mantle anisotropy, which is believed to be an intrinsic feature of the ocean lithosphere formed by seafloor spreading.

We like to interpret our observation with respect to a model where magmatically starved and tectonically disruptive lithosphere envisioned for transform faults (e.g., Detrick et al., 1993) is magmatically augmented at the proximal ridge-transform intersection before transform crust is turning into a fracture zone. Such a scenario has recently been envisioned to explain the fact that world-wide transform faults are several hundreds of meters deeper than their adjacent fracture zones and is supported by high-resolution bathymetry, showing a phase of accretion at RTIs (Grevemeyer et al., 2021). Marjanović et al. (2020) suggested that this phase of accretion is probably controlled by dyke propagation along the adjacent spreading ridge into the transform fault domain. Therefore, lithosphere found today in the St. Paul FZ has been magmatically overprinted while passing along its eastern RTI, explaining why crust along St. Paul FZ reflects magmatically accreted lithosphere.

796 **Appendix**

798 **Figure A1:** Results from Monte Carlo analysis for the line LI-02 along St. Paul FZ (Fig. 1c): **(a)** Mean
 799 initial crustal velocity model (Grevemeyer et al., 2018). **(b)** Mean final crustal velocity model obtained by
 800 cumulative inversion of Pg and PmP arrivals. The velocity contour is 1 km/s starting from 4 km/s. **(c)**
 801 Velocity deviation between mean final and mean initial model (final - initial). The contour interval is 0.2
 802 km/s starting at 0.2 km/s. **(d)** The initial standard deviation of the mean input velocity model. **(e)** The
 803 standard deviation of the final mean model. The contour interval is 0.1 km/s. **(f)** Weighted cell hits (DWS)
 804 of the final mean model. Black dots, horizontal black dashed line and grey shading denote the modelled
 805 Moho reflection points, the mean initial flat Moho and the Moho standard deviation, respectively. All
 806 remaining elements are the same as in Figure 5.

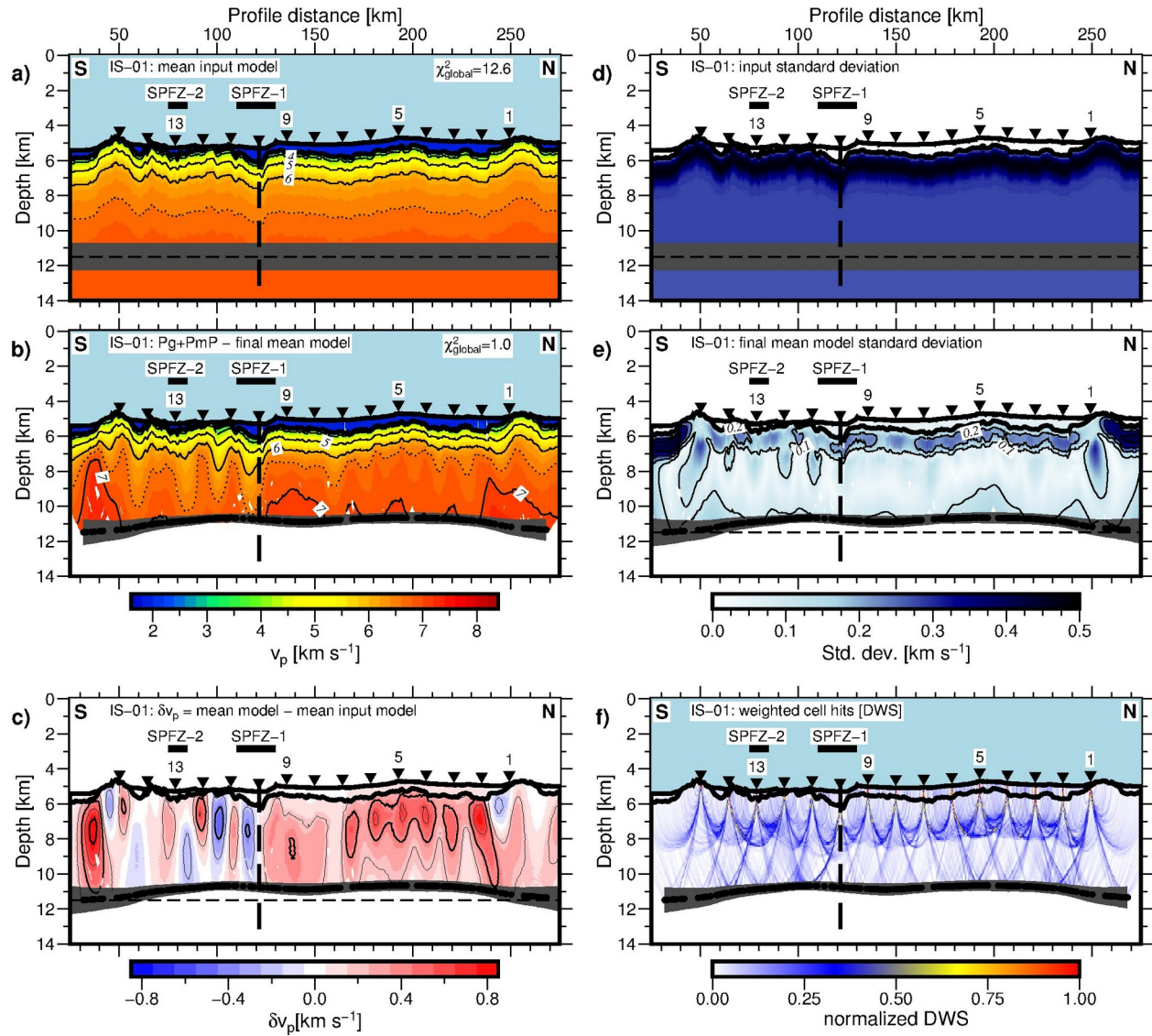


Figure A2: MCA results for line IS-01 across SPFZ (Fig. 1b): All figure elements are the same as in Figure A1 and Figure 6.

Acknowledgements

This research was funded by the German Science Foundation (DFG grant MerMET 15-93) and the European Research Council under the European Union's Seventh Framework Programme (FP7/2007-2013) under Advance Grant agreement no. 339442. We would like to thank captains and the crews of the German R/V Maria S. Merian and the French RV Pourquoi-pas? for excellent sea-going support, enabling the successful data acquisition. All figures are produced with GMT (Wessel et al., 2013). The MCS and OBS data will be made available on the Pangea open access data repository upon the acceptance of the manuscript.

References

- Ambos, E.L & Hussong D.M. (1986). Oceanographer transform fault structure compared to that of surrounding oceanic crust: Results from seismic refraction data analysis. *Journal of geodynamics*, 5.1, pp. 79–102. [https://doi.org/10.1016/0264-3707\(86\)90024-4](https://doi.org/10.1016/0264-3707(86)90024-4)
- Bell, R. E., & Buck, W. R. (1992). Crustal control of ridge segmentation inferred from observations of the Reykjanes Ridge. *Nature*, 357, 583–586. <https://doi.org/10.1038/357583a0>
- Bird, P. (2003). “An updated digital model of plate boundaries”. *Geochemistry, Geophysics, Geosystems*, 4.3. <https://doi.org/10.1029/2001GC000252>
- Bonatti, E., Seyler, M., & Sushevskaya, N. (1993)., A cold suboceanic mantle belt at the Earth equator. *Science* 261, 315-320. <https://doi.org/10.1126/science.261.5119.315>
- Cannat, M. (1993). Emplacement of mantle rocks in the seafloor at mid-ocean ridges, *Journal of Geophysical Research*, 98, 4163-4172. <https://doi.org/10.1029/92JB02221>
- Cannat, M., Mevel, C., Maia, M., Deplus, C., Durand, C., Gente, P., Agrinier, P., Belarouchi, A., Dubuisson, G., Humler, E., & Reynolds, J.(1995). Thin crust, ultramafic exposures, and rugged faulting patterns at the Mid-Atlantic Ridge (22–24° N), *Geology* 23, 49-52. [https://doi.org/10.1130/0091-7613\(1995\)023<0049:TCUEAR>2.3.CO;2](https://doi.org/10.1130/0091-7613(1995)023<0049:TCUEAR>2.3.CO;2)
- Carlson, R. L., & Miller, D. J. (2004). Influence of pressure and mineralogy on seismic velocities in oceanic gabbros: Implications for the composition and state of the lower

oceanic crust, *Journal of Geophysical Research*, 109, B09205.

<https://doi.org/10.1029/2003JB002699>

Calvert, A.J., & Potts, C.G. (1985). Seismic evidence for hydrothermally altered mantle beneath old crust in the Tydeman fracture zone. *Earth and Planetary Science Letters*, 75.4, pp. 439–449. [https://doi.org/10.1016/0012-821X\(85\)90187-6](https://doi.org/10.1016/0012-821X(85)90187-6)

Canales, J. P., Detrick, R. S., Lin, J., Collins, J. A., & Toomey, D. R. (2000). Crustal and upper mantle seismic structure beneath the rift mountains and across a nontransform offset at the Mid-Atlantic Ridge (35° N). *Journal of Geophysical Research: Solid Earth*, 105(B2), 2699–2719. <https://doi.org/10.1029/1999JB900379>

Chen, Y. J. (1992). Oceanic crustal thickness versus spreading rate. *Geophysical Research Letters*, 19(8), 753–756. <https://doi.org/10.1029/92GL00161>

Christeson, G. L., Goff, J. A., & Reece, R. S. (2019). Synthesis of oceanic crustal structure from two-dimensional seismic profiles. *Reviews of Geophysics*, 57, 504–529. <https://doi.org/10.1029/2019RG000641>

Christeson, G. L., Reece, R. S., Kardell, D. A., Estep, J. D., Fedotova, A., & Goff, J. A. (2020). South Atlantic Transect: Variations in Oceanic Crustal Structure at 31° S. *Geochemistry, Geophysics, Geosystems*, 21(7), e2020GC009017. <https://doi.org/10.1029/2020GC009017>

Cohen, J.K., Stockwell, J.W. (2010). CWP/SU: Seismic Unix Release 41: A free package for seismic research and processing: Center for Wave Phenomena, Colorado School of Mines. Available online at <https://wiki.seismic-unix.org/>

- Cormier, M. H., Detrick, R. S., & Purdy, G. M. (1984). Anomalously thin crust in oceanic fracture zones: New seismic constraints from the Kane fracture zone. *Journal of Geophysical Research: Solid Earth*, 89(B12), 10249-10266. <https://doi.org/10.1029/JB089iB12p10249>
- Creager, K. C., & Dorman, L. M. (1982). Location of instruments on the seafloor by joint adjustment of instrument and ship positions. *Journal of Geophysical Research: Solid Earth*, 87(B10), 8379-8388. <https://doi.org/10.1029/JB087iB10p08379>
- Dalton, C. A., Langmuir, C. H., & Gale, A. (2014). Geophysical and geochemical evidence for deep temperature variations beneath mid-ocean ridges. *Science*, 344(6179), 80-83. <https://www.doi.org/10.1126/science.1249466>
- Dannowski, A., Grevemeyer, I., Phipps Morgan, J., Ranero, C. R., Maia, M., & Klein, G. (2011). Crustal structure of the propagating TAMMAR ridge segment on the Mid-Atlantic Ridge, 21.5 N. *Geochemistry, Geophysics, Geosystems*, 12(7). <https://doi.org/10.1029/2011GC003534>
- Dannowski, A., Morgan, J. P., Grevemeyer, I., & Ranero, C. R. (2018). Enhanced mantle upwelling/melting caused segment propagation, oceanic core complex die off, and the death of a transform fault: The Mid-Atlantic Ridge at 21.5 N. *Journal of Geophysical Research: Solid Earth*, 123(2), 941-956. <https://doi.org/10.1002/2017JB014273>
- Davy, R. G., Collier, J. S., Henstock, T. J., VoiLA Consortium, Rietbrock, A., Goes, S., et al. (2020). Wide-angle seismic imaging of two modes of crustal accretion in mature

Atlantic Ocean crust. *Journal of Geophysical Research: Solid Earth*, 125(6),
e2019JB019100. <https://doi.org/10.1029/2019JB019100>

de Melo, G. W., Parnell-Turner, R., Dziak, R. P., Smith, D. K., Maia, M., do Nascimento,
A. F., & Royer, J. Y. (2021). Uppermost Mantle Velocity beneath the Mid-Atlantic
Ridge and Transform Faults in the Equatorial Atlantic Ocean. *Bulletin of the
Seismological Society of America*, 111(2), 1067-1079.
<https://doi.org/10.1785/0120200248>

Detrick Jr, R. S., & Purdy, G. M. (1980). The crustal structure of the Kane fracture zone
from seismic refraction studies. *Journal of Geophysical Research: Solid Earth*, 85(B7),
3759-3777. <https://doi.org/10.1029/JB085iB07p03759>

Detrick, R. S., Cormier, M. H., Prince, R. A., Forsyth, D. W., & Ambos, E. L. (1982).
Seismic constraints on the crustal structure within the Vema fracture zone. *Journal of
Geophysical Research: Solid Earth*, 87(B13), 10599-10612.
<https://doi.org/10.1029/JB087iB13p10599>

Detrick, R. S., White, R. S., & Purdy, G. M. (1993). Crustal structure of North Atlantic
fracture zones. *Reviews of Geophysics*, 31(4), 439-458.
<https://doi.org/10.1029/93RG01952>

Dunn, R. A., & Toomey, D. R. (1997). Seismological evidence for three-dimensional melt
migration beneath the East Pacific Rise. *Nature*, 388(6639), 259-262.
<https://doi.org/10.1038/40831>

- Dunn, R. A., & Toomey, D. R. (2001). Crack-induced seismic anisotropy in the oceanic crust across the East Pacific Rise (9° 30' N). *Earth and Planetary Science Letters*, 189(1-2), 9-17. [https://doi.org/10.1016/S0012-821X\(01\)00353-3](https://doi.org/10.1016/S0012-821X(01)00353-3)
- Dunn, R. A., Toomey, D. R., & Solomon, S. C. (2000). Three-dimensional seismic structure and physical properties of the crust and shallow mantle beneath the East Pacific Rise at 9° 30'N. *Journal of Geophysical Research: Solid Earth*, 105(B10), 23537-23555. <https://doi.org/10.1029/2000JB900210>
- Gaherty, J. B., Lizarralde, D., Collins, J. A., Hirth, G., & Kim, S. (2004). Mantle deformation during slow seafloor spreading constrained by observations of seismic anisotropy in the western Atlantic. *Earth and Planetary Science Letters*, 228(3-4), 255-265. <https://doi.org/10.1016/j.epsl.2004.10.026>
- Gregory, E., Singh, S. C., Marjanović, M., & Wang, Z. (2021). Serpentinized peridotite versus thick mafic crust at the Romanche oceanic transform fault, *Geology*, in press
- Grevenmeyer, I. (2020). Upper Mantle Structure beneath the Mid-Atlantic Ridge from Regional Waveform Modeling. *Bulletin of the Seismological Society of America*, 110(1), 18-25. <https://doi.org/10.1785/0120190080>
- Grevenmeyer, I., Kaul, N., Villinger, H., & Weigel, W. (1999). Hydrothermal activity and the evolution of the seismic properties of upper oceanic crust. *Journal of Geophysical Research: Solid Earth*, 104(B3), 5069-5079. <https://doi.org/10.1029/1998JB900096>
- Grevenmeyer, I., Ranero, C. R., & Ivandic, M. (2018). Structure of oceanic crust and serpentinization at subduction trenches. *Geosphere*, 14(2), 395-418. <https://doi.org/10.1130/GES01537.1>

- Grevenmeyer, I., Rüpke, L.H., Morgan, J.P., Iyer, K., & Devey, C.W. (2021). Extensional tectonics and two-stage crustal accretion at oceanic transform faults. *Nature*, 591, 402–407. <https://doi.org/10.1038/s41586-021-03278-9>
- Grion, S., Exley, R., Manin, M., Miao, X., Pica, A. L., Wang, Y., et al. (2007). Mirror imaging of OBS data. *first break*, 25(11). <https://doi.org/10.3997/1365-2397.2007028>
- Harding, J. L., Van Avendonk, H. J., Hayman, N. W., Grevenmeyer, I., Peirce, C., & Dannowski, A. (2017). Magmatic-tectonic conditions for hydrothermal venting on an ultraslow-spread oceanic core complex. *Geology*, 45(9), 839-842. <https://doi.org/10.1130/G39045.1>
- Hooft, E. E. E., Detrick, R. S., Toomey, D. R., Collins, J. A., & Lin, J. (2000). Crustal thickness and structure along three contrasting spreading segments of the Mid-Atlantic Ridge, 33.5–35 N. *Journal of Geophysical Research: Solid Earth*, 105(B4), 8205-8226. <https://doi.org/10.1029/1999JB900442>
- James, E. K., Dalton, C. A., & Gaherty, J. B. (2014). Rayleigh wave phase velocities in the Atlantic upper mantle. *Geochemistry, Geophysics, Geosystems*, 15(11), 4305-4324. <https://doi.org/10.1002/2014GC005518>
- Korenaga, J., Holbrook, W. S., Kent, G. M., Kelemen, P. B., Detrick, R. S., Larsen, H. C., et al. (2000). Crustal structure of the southeast Greenland margin from joint refraction and reflection seismic tomography. *Journal of Geophysical Research: Solid Earth*, 105(B9), 21591-21614. <https://doi.org/10.1029/2000JB900188>

- Korenaga, J., Kelemen, P. B., & Holbrook, W. S. (2002). Methods for resolving the origin of large igneous provinces from crustal seismology. *Journal of Geophysical Research: Solid Earth*, 107(B9), ECV-1. <https://doi.org/10.1029/2001JB001030>
- Lin, J., Purdy, G. M., Schouten, H., Sempere, J. C., & Zervas, C. (1990). Evidence from gravity data for focused magmatic accretion along the Mid-Atlantic Ridge. *Nature*, 344(6267), 627-632. <https://doi.org/10.1038/344627a0>
- Lin, J., & Morgan, J. P. (1992). The spreading rate dependence of three-dimensional mid-ocean ridge gravity structure. *Geophysical Research Letters*, 19(1), 13-16. <https://doi.org/10.1029/91GL03041>
- Macdonald, K. C., Fox, P. J., Perram, L. J., Eisen, M. F., Haymon, R. M., Miller, S. P., et al. (1988). A new view of the mid-ocean ridge from the behaviour of ridge-axis discontinuities. *Nature*, 335(6187), 217-225. <https://doi.org/10.1038/335217a0>
- Maia, M., Sichel, S., Briais, A., Brunelli, D., Ligi, M., Ferreira, N., et al. (2016). Extreme mantle uplift and exhumation along a transpressive transform fault. *Nature Geoscience*, 9(8), 619-623. <https://doi.org/10.1038/ngeo2759>
- Marjanović, M., Singh, S. C., Gregory, E. P., Grevemeyer, I., Growe, K., Wang, Z., et al. (2020). Seismic crustal structure and morphotectonic features associated with the Chain Fracture Zone and their role in the evolution of the equatorial Atlantic region. *Journal of Geophysical Research: Solid Earth*, 125(10), e2020JB020275. <https://doi.org/10.1029/2020JB020275>

Matthews, K. J., Müller, R. D., Wessel, P., & Whittaker, J. M. (2011). The tectonic fabric of the ocean basins. *Journal of Geophysical Research: Solid Earth*, 116(B12).

<https://doi.org/10.1029/2011JB008413>

McKenzie, D. P., & Parker, R. L. (1967). The North Pacific: an example of tectonics on a sphere. *Nature*, 216(5122), 1276-1280. <https://doi.org/10.1038/2161276a0>

Mckenzie, D. A. N., & Bickle, M. J. (1988). The volume and composition of melt generated by extension of the lithosphere. *Journal of petrology*, 29(3), 625-679.

<https://doi.org/10.1093/petrology/29.3.625>

Mehouachi, F., & Singh, S. C. (2018). Water-rich sublithospheric melt channel in the equatorial Atlantic Ocean. *Nature Geoscience*, 11(1), 65-69.

<https://doi.org/10.1038/s41561-017-0034-z>

Menard, H. W. (1967). Extension of northeastern-Pacific fracture zones. *Science*, 155(3758), 72-74. <https://doi.org/10.1126/science.155.3758.72>

Menard, H. W. (1955). Deformation of the northeastern Pacific basin and the west coast of North America. *Geological Society of America Bulletin*, 66(9), 1149-1198.

[https://doi.org/10.1130/0016-7606\(1955\)66\[1149:DOTNPB\]2.0.CO;2](https://doi.org/10.1130/0016-7606(1955)66[1149:DOTNPB]2.0.CO;2)

Minshull, T. A., White, R. S., Mutter, J. C., Buhl, P., Detrick, R. S., Williams, C. A., & Morris, E. (1991). Crustal structure at the Blake Spur fracture zone from expanding spread profiles. *Journal of Geophysical Research: Solid Earth*, 96(B6), 9955-9984.

<https://doi.org/10.1029/91JB00431>

- Morgan, W. J. (1968). Rises, trenches, great faults, and crustal blocks. *Journal of Geophysical Research*, 73(6), 1959-1982. <https://doi.org/10.1029/JB073i006p01959>
- Morgan, J. P., & Parmentier, E. M. (1984). Lithospheric stress near a ridge-transform intersection. *Geophysical Research Letters*, 11(2), 113-116. <https://doi.org/10.1029/GL011i002p00113>
- Moser, T. J. (1991). Shortest path calculation of seismic rays. *Geophysics*, 56(1), 59-67. <https://doi.org/10.1190/1.1442958>
- Moser, T. J., Nolet, G., & Snieder, R. (1992). Ray bending revisited. *Bulletin of the Seismological Society of America*, 82(1), 259-288.
- Müller, R. D., Sdrolias, M., Gaina, C., & Roest, W. R. (2008). Age, spreading rates, and spreading asymmetry of the world's ocean crust. *Geochemistry, Geophysics, Geosystems*, 9(4). <https://doi.org/10.1029/2007GC001743>
- Muller, M. R., Minshull, T. A., & White, R. S. (1999). Segmentation and melt supply at the Southwest Indian Ridge. *Geology*, 27(10), 867-870. [https://doi.org/10.1130/0091-7613\(1999\)027<0867:SAMSAT>2.3.CO;2](https://doi.org/10.1130/0091-7613(1999)027<0867:SAMSAT>2.3.CO;2)
- Niu, X., Ruan, A., Li, J., Minshull, T. A., Sauter, D., Wu, Z., et al. (2015). Along-axis variation in crustal thickness at the ultraslow spreading Southwest Indian Ridge (50° E) from a wide-angle seismic experiment. *Geochemistry, Geophysics, Geosystems*, 16(2), 468-485. <https://doi.org/10.1002/2014GC005645>

Paige, C. C., & Saunders, M. A. (1982). LSQR: An algorithm for sparse linear equations and sparse least squares. *ACM Transactions on Mathematical Software (TOMS)*, 8(1), 43-71.

Peirce, C., Reveley, G., Robinson, A. H., Funnell, M. J., Searle, R. C., Simão, N. M., et al. (2019). Constraints on crustal structure of adjacent OCCs and segment boundaries at 13° N on the Mid-Atlantic Ridge. *Geophysical Journal International*, 217(2), 988-1010. <https://doi.org/10.1093/gji/ggz074>

Planert, L., Flueh, E. R., & Reston, T. J. (2009). Along-and across-axis variations in crustal thickness and structure at the Mid-Atlantic Ridge at 5 S obtained from wide-angle seismic tomography: Implications for ridge segmentation. *Journal of Geophysical Research: Solid Earth*, 114(B9). <https://doi.org/10.1029/2008JB006103>

Potts, C. G., Calvert, A. J., & White, R. S. (1986). Crustal structure of Atlantic fracture zones-III. The Tydeman fracture zone. *Geophysical Journal International*, 86(3), 909-942. <https://doi.org/10.1111/j.1365-246X.1986.tb00668.x>

Purdy, G. M. (1983). The seismic structure of 140 Myr old crust in the western central Atlantic Ocean. *Geophysical Journal International*, 72(1), 115-137. <https://doi.org/10.1111/j.1365-246X.1983.tb02808.x>

Raïtt, M. (1963). The crustal rocks. *The sea*, 3, 85-102.

Roland, E., Lizarralde, D., McGuire, J. J., & Collins, J. A. (2012). Seismic velocity constraints on the material properties that control earthquake behavior at the Quebrada-Discovery-Gofar transform faults, East Pacific Rise. *Journal of Geophysical Research: Solid Earth*, 117(B11). <https://doi.org/10.1029/2012JB009422>

- Sandwell, D. T. (1984). Thermomechanical evolution of oceanic fracture zones. *Journal of Geophysical Research: Solid Earth*, 89(B13), 11401-11413.
<https://doi.org/10.1029/JB089iB13p11401>
- Sandwell, D. T., Müller, R. D., Smith, W. H., Garcia, E., & Francis, R. (2014). New global marine gravity model from CryoSat-2 and Jason-1 reveals buried tectonic structure. *Science*, 346(6205), 65-67. <https://doi.org/10.1126/science.1258213>
- Searle, R. C., Thomas, M. V., & Jones, E. J. W. (1994). Morphology and tectonics of the Romanche Transform and its environs. *Marine Geophysical Researches*, 16(6), 427-453. <https://doi.org/10.1007/BF01270518>
- Sykes, L. R. (1967). Mechanism of earthquakes and nature of faulting on the mid-oceanic ridges. *Journal of Geophysical Research*, 72(8), 2131-2153.
<https://doi.org/10.1029/JZ072i008p02131>
- Taylor, M. A. J., & Singh, S. C. (2002). Composition and microstructure of magma bodies from effective medium theory. *Geophysical Journal International*, 149(1), 15-21.
<https://doi.org/10.1046/j.1365-246X.2002.01577.x>
- Tolstoy, M., Harding, A. J., & Orcutt, J. A. (1993). Crustal thickness on the Mid-Atlantic Ridge: Bull's-eye gravity anomalies and focused accretion. *Science*, 262(5134), 726-729. <https://doi.org/10.1126/science.262.5134.726>
- Toomey, D. R., & Foulger, G. R. (1989). Tomographic inversion of local earthquake data from the Hengill-Grensdalur central volcano complex, Iceland. *Journal of Geophysical*

Research: Solid Earth, 94(B12), 17497-17510.

<https://doi.org/10.1029/JB094iB12p17497>

Van Avendonk, H. J., Davis, J. K., Harding, J. L., & Lawver, L. A. (2017). Decrease in oceanic crustal thickness since the breakup of Pangaea. *Nature Geoscience*, 10(1), 58-61. <https://doi.org/10.1038/ngeo2849>

Vaddineni, V. A., Singh, S.C., Grevemeyer, I., Audhkhasi, P., & Papenberg, C. (2021). Evolution of the Crustal and upper Mantle seismic structure from 0-27 Ma in the equatorial Atlantic Ocean at 2°43'S, *Journal of Geophysical Research: Solid Earth*, revised

Vine, F. J., & Moores, E. M. (1972). A model for the gross structure, petrology, and magnetic properties of oceanic crust. *Studies in Earth and Space Sciences: A Memoir in Honor of Harry Hammond Hess*, 195-205.

Wessel, P., Smith, W. H., Scharroo, R., Luis, J., & Wobbe, F. (2013). Generic mapping tools: improved version released. *Eos, Transactions American Geophysical Union*, 94(45), 409-410. <https://doi.org/10.1002/2013EO450001>

White, R. S., Detrick, R. S., Sinha, M. C., & Cormier, M. H. (1984). Anomalous seismic crustal structure of oceanic fracture zones. *Geophysical Journal International*, 79(3), 779-798. <https://doi.org/10.1111/j.1365-246X.1984.tb02868.x>

White, R. S., McKenzie, D., & O'Nions, R. K. (1992). Oceanic crustal thickness from seismic measurements and rare earth element inversions. *Journal of Geophysical Research: Solid Earth*, 97(B13), 19683-19715. <https://doi.org/10.1029/92JB01749>

1141

1142

Whitmarsh, R. B. (1978). Seismic refraction studies of the upper igneous crust in the North

1143

Atlantic and porosity estimates for layer 2. *Earth and Planetary Science Letters*, 37(3),

1144

451-464. [https://doi.org/10.1016/0012-821X\(78\)90061-4](https://doi.org/10.1016/0012-821X(78)90061-4)

1145

1146

Whitmarsh, R. B., & Calvert, A. J. (1986). Crustal structure of Atlantic fracture zones—I.

1147

The Charlie-Gibbs fracture zone. *Geophysical Journal International*, 85(1), 107-138.

1148

<https://doi.org/10.1111/j.1365-246X.1986.tb05174.x>

1149

1150

Wilson, J. T. (1965). A new class of faults and their bearing on continental drift. *Nature*,

1151

207(4995), 343-347.

1152

1153

Yilmaz, Ö. (2001). *Seismic data analysis: Processing, inversion, and interpretation of*

1154

seismic data. Society of exploration geophysicists.